

Topographic Effects on Internal Waves at Barkley Canyon

Kurtis Anstey

V00939802

Department of Physics and Astronomy

University of Victoria

January 28, 2022

Dr. Jody Klymak (University of Victoria)

Dr. Steven Mihaly (Ocean Networks Canada)

Dr. Richard Thomson (Institute of Ocean Sciences)

Table of Contents

List of Figures	3
1 Abstract	4
2 Introduction	5
3 Internal wave theory	8
4 Barkley Canyon	12
5 Results	18
5.1 Observations	18
5.1.1 Mean currents	18
5.1.2 High frequency currents	18
5.1.3 Depth dependence	22
5.2 Frequency-dependent response	24
5.2.1 Sub-diurnal	24
5.2.2 Diurnal	26
5.2.3 Near-inertial	29
5.2.4 Semidiurnal	33
5.2.5 Continuum	36
5.2.6 Shoulder	42
6 Discussion	45
6.1 Canyon axis mean currents	45
6.2 Tidal forcing	46
6.3 Near-inertial forcing	49
6.4 Continuum-dissipation estimates	51
6.5 Spectral shoulder energy	52
7 Summary and conclusions	53
8 Appendix A: Supplemental plots	56
8.1 Wind comparisons	56
9 References	59

List of Figures

1	IW processes	6
2	IW in a two-layer system	7
3	IW and topography	8
4	Barkley Canyon site map and semidiurnal criticality	9
5	Site topography	10
6	ADCP frequency, instrument ID, deployment, and data availability	13
7	QA threshold profiles	14
8	Mean stratification and WKB scaling factor	15
9	Low-pass velocities	17
10	Axis along-canyon mean-flow	19
11	High-pass velocities - April 2013	20
12	PSD and rotary spectra	21
13	Depth-frequency PSD	23
14	Depth-band PSD - Sub-diurnal	25
15	Depth-band PSD - Diurnal	27
16	Diurnal spring-neap forcing	28
17	Depth-band rotary PSD - Near-inertial	30
18	NI vertical energy propagation	31
19	NI delayed deep response histogram	31
20	NI slab response - 2013	32
21	NI vertical modes	33
22	Depth-band PSD - Semidiurnal	34
23	Semidiurnal spring-neap forcing	35
24	Depth-band PSD - Continuum	37
25	Continuum power law fits	38
26	Dissipation and diffusivity	39
27	Dissipation power law fits	40
28	Dissipation multi-variate power law fits	42
29	Depth-band PSD - Shoulder	43
30	Shoulder-dissipation power law fits	44
31	High frequency-resolution PSD - 2013	50
32	Appendix A - NI wind comparisons - 2014	56
33	Appendix A - NI wind comparisons - 2017	57
34	Appendix A - NI wind comparisons - 2018	58

1 Abstract

At two Barkley Canyon sites (the continental slope below the shelf-break, and deep within the canyon), four overlapping years of horizontal velocity time-series data are used to examine the effects of irregular topography on the internal wave field. Mean currents are topographically guided at both sites, and in the canyon there is an inter-annually consistent, periodic (about a week) up-canyon flow (-700 to -900 m) above a near-bottom down-canyon layer. There is elevation of internal wave energy near topography, up to a factor of 10, 130 m above the slope, and up to a factor of 100, 230 m above the canyon bottom. All bands display inter-annually consistent, frequency-dependent seasonality. Sub-diurnal and diurnal flows are sub-inertially trapped along topography, and the diurnal band appears to be forced locally (barotropically). Both sites have high NI energy. At the slope site, NI energy is attenuated with depth, while in the canyon NI energy is amplified near the bottom. Both sites show intermittent NI forcing associated with wind events, high-mode propagation, and the seasonal mixed-layer depth, though fewer events are observed in the canyon. Free semidiurnal internal tides are focused and reflected near critical shelf-break and canyon floor topography, and appear to experience both local and remote (baroclinic) forcing. The high-frequency internal wave continuum has enhanced amplitudes near bottom at both sites (up to 7× open-ocean GM), and inferred dissipation rates, ϵ , increasing from a background of less than 10^{-9} W/kg to exceeding 10^{-8} W/kg. Dissipation is most strongly correlated with the semidiurnal (M_2) constituent at both sites, with secondary contributions from the sub-diurnal (Sub_{K1}) band on the slope, and the NI band in the canyon. Power laws for these dependencies are $\epsilon \sim M_2^{0.83} + \text{Sub}_{K1}^{0.59}$ at the slope, and $\epsilon \sim M_2^{1.47} + \text{NI}^{0.24}$ in the canyon. There is evidence of a near- N spectral shoulder correlated with continuum energy, with a power law fit of $P_{Sh} \sim \epsilon^{0.34 \pm 0.08}$ that is independent of site topography. Though some general results are expected from observations at other slope and canyon sites, it seems that regional characteristics may make for unique, site-dependent forcing of internal wave driven processes.

2 Introduction

Internal waves (IW) are slow-moving, low-frequency, sub-surface gravity waves that exist within density gradients in the ocean interior (Garrett & Munk, 1979). They have horizontal wavelengths up to kilometres long, and oscillate in a range between the local Coriolis (inertial, f) and Brunt–Väisälä (buoyancy, N) frequencies (Garrett & Munk, 1979). They are forced by weather - as near-inertial (NI) IW generated by surface winds exciting currents in the mixed layer (ML) that pump energy into the interior (Garratt, 1977) - or by tides and currents moving across irregular seafloor topography, generating baroclinic internal tides (IT) and IW that can propagate through the stratified ocean (Hendershott & Garrett, 2018). As travelling IW approach irregular topography, such as continental slopes or submarine canyons, they can focus and break, leading to elevated mixing. As mixing can be linked to ocean circulation, biogeochemical cycles, weather, and long-term climate (Kunze, 2017), it is important to understand forcing by the IW field. As incident IW and IT have varying origins, amplitudes, and frequencies, each responds differently to the influence of impacted topography. Sub-inertial IW and IT may be trapped along topography, while those that are NI or super-inertial are free to reflect and propagate through open water. By characterising the IW and IT that comprise the local IW field, it may be possible to better quantify and understand IW driven turbulence and mixing.

The wind, currents, and tides are ever-present, and IW are prevalent ocean phenomena. As early as the mid-19th century, notable scientists such as Stokes and Rayleigh were investigating properties of fluid density and stratification, essential for IW propagation (Garrett & Munk, 1979). IW were mistaken as consistent noise in early 20th-century hydrocast readings, and Ekman discussed their effects in his seminal theories on fluid mechanics (Garrett & Munk, 1979). In the late-20th century, Garrett and Munk (1979) developed the canonical Garrett-Munk (GM) spectrum defining the characteristic frequency and wavenumber continuum of open-ocean IW, to better understand their role in ocean processes. Instrumentation improved, and scientists continued to uncover the contributions of IW to physical systems of all scales, from fine-scale mixing to the large-scale meridional overturning circulation (Figure 1; Garrett & Munk, 1979). Recently, studies have linked IW generation and dissipation to the global oceanic energy budget (Carter & Gregg, 2002; Kunze et al., 2002; Terker et al., 2014; Kunze, 2017), tide and wind forcing of IW to seasonal variability of regional circulation processes (Alford et al., 2012; Thomson & Krassovski, 2015), and enhanced mixing to IW interactions with irregular topography (Nash et al., 2004; Kunze et al., 2012; Gemmrich & Klymak, 2015).

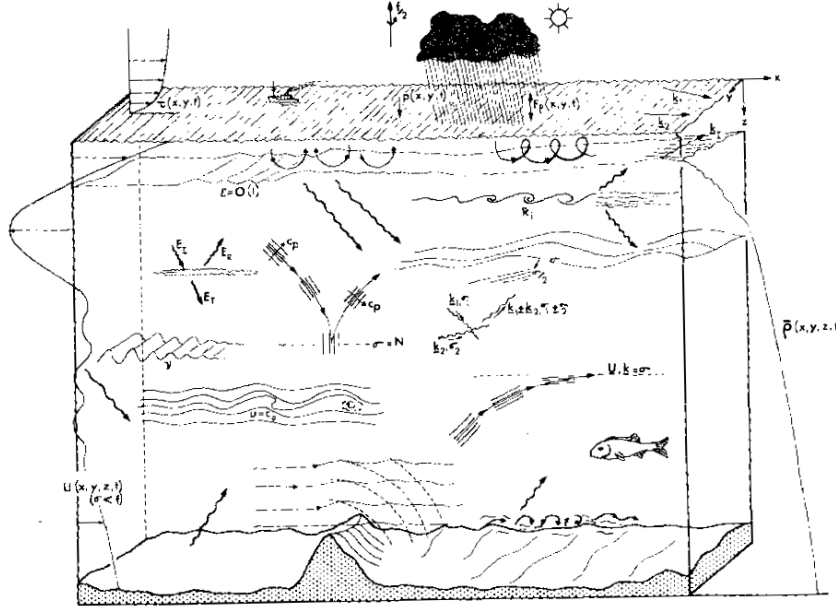


Figure 1. Generalised depiction of IW processes in the ocean, as envisioned by Garrett and Munk (1979). IW are forced by, coincide with, or contribute to most physical processes in the ocean.

Further research on IW interactions with irregular topography is thought to be essential to understanding seasonal upwelling, diapycnal mixing, and cross-shelf exchange (Burrier, 2019). As IW and IT approach seamounts, slopes, or canyons, nonlinear processes may cause their energy to reflect, scatter, or focus and break (Figure 3), dissipating as heat (Garrett & Munk, 1979; Klymak et al., 2006; Kunze et al., 2012). Dissipation leads to an energetic local environment, evident as near-bottom turbulent processes on the fine- (1 - 100 m vertical) and micro-scales (< 1 m vertical) (Garrett & Munk, 1979; Carter & Gregg, 2002; Kunze et al., 2002; Kunze et al., 2012). These processes lead to the elevated mixing of pollutants and biological constituents, and drive regional transport of energy and momentum (Kunze et al., 2012). Topography-forced IW mixing helps set ocean stratification, layers that even influence the large-scale ocean-atmosphere coupled climate system (Garett & Munk, 1979).

In Canada, IW are regularly observed on the highly productive Vancouver Island Continental Shelf (VICS) (Thomson & Crawford, 1982; Allen et al., 2001), a relatively broad (about 80 km) shelf region featuring a canyon-incised continental slope. Regional observations have led to insight on non-linear wave-wave interactions between surface generated NI IW and upward propagating semidiurnal IT (Mihaly et al., 1998), and the presence of diurnal baroclinic shelf waves forced by tidal oscillations near the mouth of the Juan de

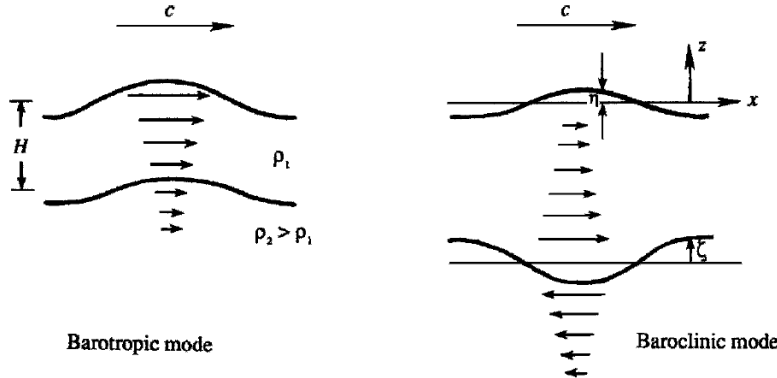


Figure 2. IW in a two-layer system. Graphic representation of the difference between barotropic and baroclinic flows. Adapted from Kundu & Cohen (2008).

Fuca Strait (Thomson & Crawford, 1982). Seasonally variable regional currents (Thomson & Krassovski, 2015) have been associated with observations of vorticity stretching and upwelling at the head of the shelf-incising Barkley Canyon, suggesting considerable canyon influence on VICS water properties, transport of biological constituents, and overall shelf productivity (Allen et al., 2001; Juniper et al., 2013; Doya et al., 2013; Chauvet et al., 2018). However, there is a lack of topography-IW observations at Barkley Canyon necessary to properly characterise its influence on the physical processes of the VICS. Further research into Barkley Canyon's IW field can provide insight into the effects of topography-driven mixing on the productivity of not only the VICS, but global shelf sites adjacent to canyon-incised continental slopes.

This study evaluates horizontal velocity data from two Barkley Canyon sites, one on the adjacent continental slope and one within the canyon, to characterise the topography interactions of IW and IT, and their potential influence on local mixing. Mean currents, and IW of sub-tidal, tidal, NI, and super-tidal (IW continuum and near- N spectral shoulder) frequency bands are evaluated for depth-dependence and seasonality, including a forcing analysis of variability due to regional currents, tides, and wind. The high-frequency IW continuum is evaluated for topographic influence by comparison with open-ocean GM theory, leading to approximations of dissipation and diffusivity to estimate mixing. The seasonal energy of the continuum is correlated to low-frequency constituents to identify which bands contribute most to high-frequency turbulent processes. Key findings include deep-canyon topography-guided current layers, near-topography focusing of IW energy with frequency-dependent seasonality and forcing, attenuation of downward NI IW energy above the

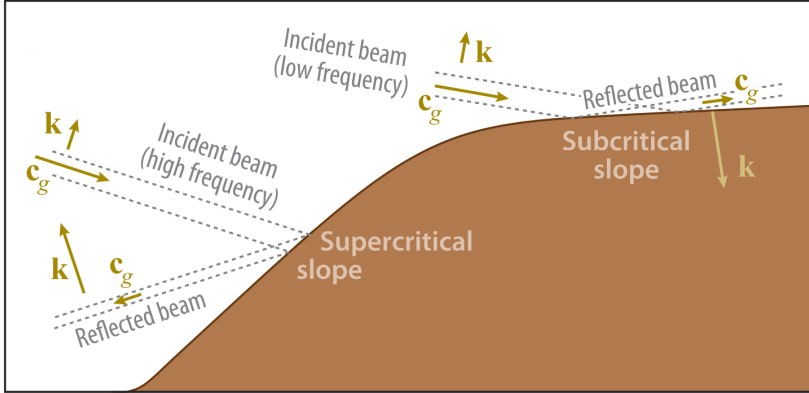


Figure 3. Graphic of IW interactions with slope topography (Lamb, 2014). The propagation angle of an IW depends on frequency and stratification. Depending on the slope of topography, incident IW can be scattered up, reflected down, or focused, possibly breaking.

continental slope, elevated high-frequency IW continuum energy linked to the semidiurnal constituent, and an energetic near- N spectral shoulder that is seasonally correlated with continuum energy.

3 Internal wave theory

Vertical displacements in a fluid can be classified as either barotropic, where the displacement is dependent only on pressure, $P(z)$ (where z is depth), or as baroclinic, where the displacement is also a function of density, $\rho(z)$, temperature, $T(z)$, etc. (Figure 2). For example, surface tides are barotropic, affecting most of the water column as the surface oscillates, while IW are baroclinic, perturbations that exist along density interfaces in the stratified ocean interior. IW are highly dependent on stratification, characterised by the depth-dependent buoyancy frequency, $N(z)$, defined as:

$$N^2(z) = -\frac{g}{\rho_0} \frac{d\rho}{dz} \quad (1)$$

where g is the acceleration due to gravity, and ρ_0 a constant reference density. In continuously stratified fluids such as the ocean interior, IW may exist both non-isotropically and rotationally, with the relative effects of clockwise (CW) and counter-clockwise (CCW) rotation described by the consistency relation:

$$\frac{CW}{CCW} = \frac{(\omega + f)^2}{(\omega - f)^2} \quad (2)$$

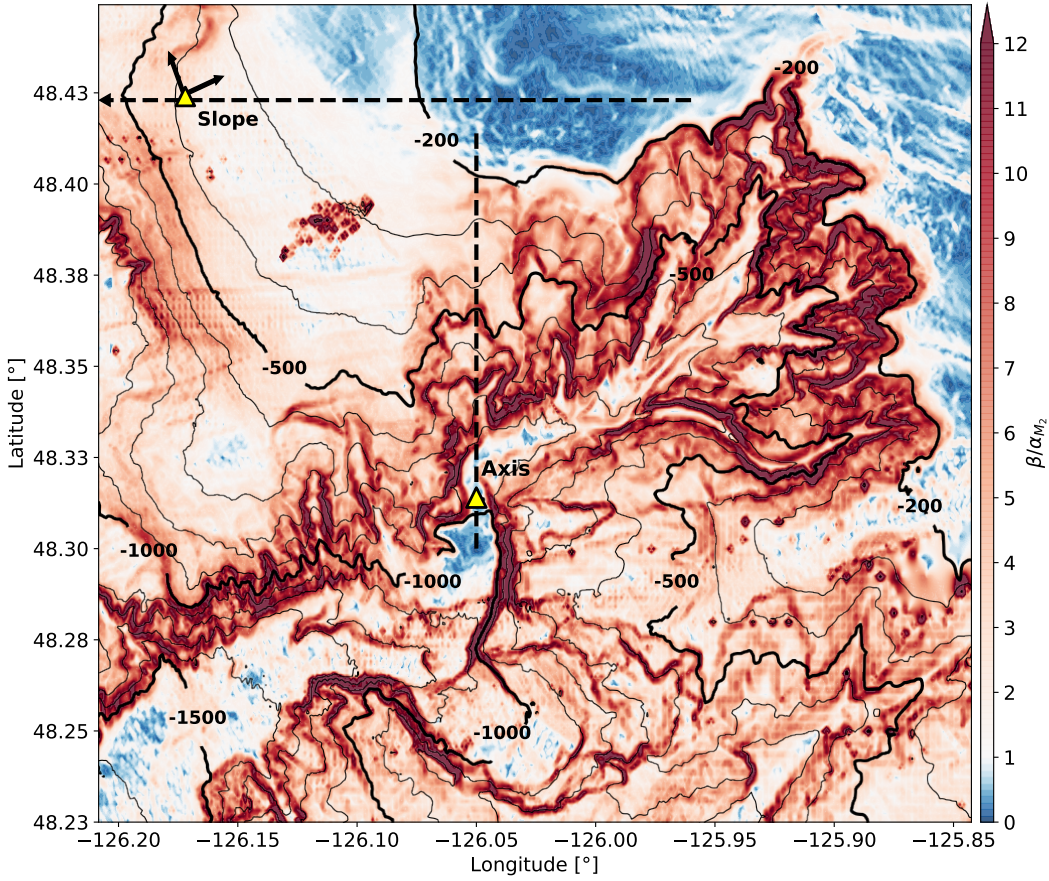


Figure 4. Site map and semidiurnal criticality of Barkley Canyon. Criticality is found by dividing the gradient slope (β) of topography by the depth-dependent semidiurnal propagation angle (α_{M_2}). Most of the region is supercritical (> 1) to the M_2 IT, with notable exceptions on the shelf and canyon floor near the Axis site. Arrows at the Slope site indicate 30° rotation of velocity data to match approximate along-slope (v) direction of mean currents; Axis data were not rotated, as the along-canyon (v) component is aligned N-S. Dashed black lines indicate topography cross-sections used in Figure 5.

where ω is frequency, and f the Coriolis frequency ($f = 2\Omega \sin \phi$, where Ω is the rotation rate of the Earth, and ϕ is latitude). f and $N(z)$ are the lower and upper frequency bounds for free IW (Kundu & Cohen, 2008). IW generated outside this frequency range are evanescent (trapped) to topography, unable to radiate into the ocean interior (Flather, 1988).

As free IW and IT approach irregular topography (continental slopes, canyons, etc.), the angle of the incident wave ray, α , and the slope of the topography, β , have an influential relationship on the behaviour of the topography-IW interaction (Figure 3) (Lamb, 2014). The ray path of an incident, free IW in

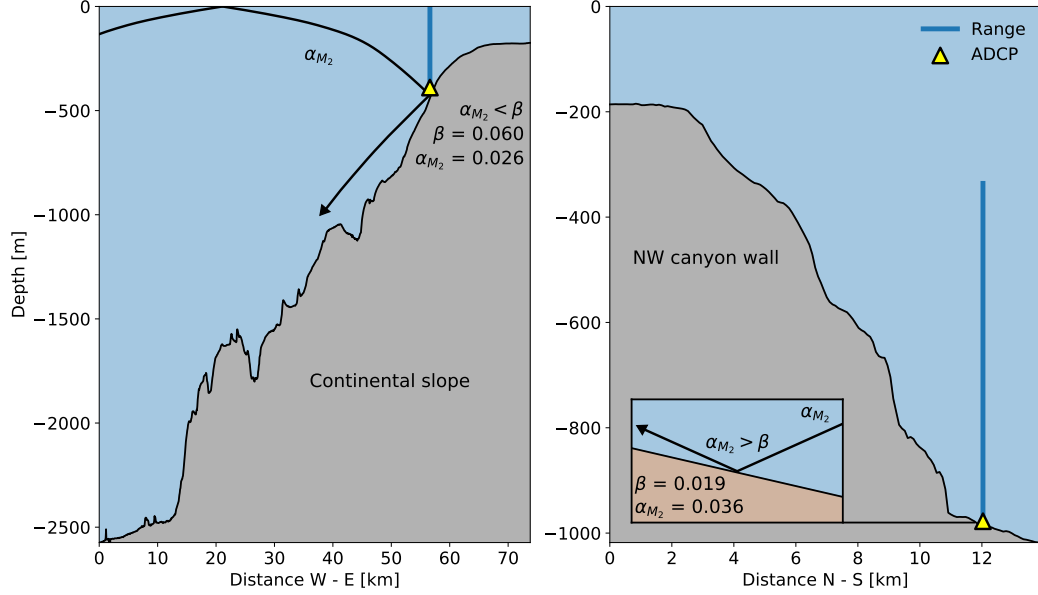


Figure 5. Site topography cross-sections with ray tracing. Depicted are the relative locations for Slope (left) and Axis (right) instrument moorings. Horizontal cross-sections were taken in the W-E (Slope) and N-S (Axis) directions, represented by the dashed black lines in Figure 4. Slope sits below the VICS shelf-break while Axis is located on the floor of Barkley Canyon (right). An incident ray is shown for M_2 , accounting for depth-dependent stratification, as well as local criticality at each site. α is the angle of propagation, and β is the slope of the topography. In general, the Slope region is supercritical, while the Axis region is both subcritical (floor) and supercritical (walls).

a continuously stratified fluid is (Nash et al., 2004; Garrett & Kunze, 2007; Lamb, 2014):

$$\alpha(z) = \sqrt{\frac{(\omega^2 - f^2)}{(N(z)^2 - \omega^2)}} \quad (3)$$

The impacted bathymetric slope, $\beta = \nabla H$, is determined from the gradient magnitude of the local topography, and used to determine regions of IW and IT criticality, as in Figure 4 (Martini et al., 2011). As α depends on $N(z)$, the characteristic ray path of an IW bends with depth. If $\beta > \alpha$, the slope is supercritical and incident wave energy is reflected downward (see Figure 5); for $\beta \approx \alpha$, the slope is near-critical and incident wave energy is focused, potentially leading to non-linear breaking and dissipation; and, for $\beta < \alpha$, the slope is considered subcritical and incident wave energy is scattered upward (Klymak et al., 2011). The combined effects of reflection, scattering, and focusing of IW and IT in near-critical regions can lead to an energetic layer near topography (Lamb, 2014). Intensified near-slope layers are not uncommon (Polzin et al., 1997; Nash et al., 2004; Kunze et al., 2012), and can elevate IW energy multiple

orders of magnitude with depth-dependent vertical scales hundreds of metres above bottom (Hotchkiss & Wunsch, 1982; Gemmrich & Klymak, 2015), in turn elevating mixing.

The energetic mixing regions near-critical to tidal frequencies are also known as hot-spots for generation of baroclinic IT, including continental slope, shelf-break, and canyon topography, though IT can also be generated over non-critical irregular topography through frictional tidal oscillations (Garrett & Kunze, 2007). Topographically generated free IT can radiate away baroclinically, potentially impacting distant topography, dissipating their energy remotely (Kunze et al., 2012). At latitudes where an oscillating tidal frequency is sub-inertial and generated IT are trapped to topography, baroclinic 'shelf waves' may be generated over irregular topography and propagate along the continental margin where the topographic gradient of the shelf acts as a restoring force for horizontal propagation (Crawford & Thomson, 1984; Brink, 1991).

In addition to topographically generated IW and IT, there is significant input into the oceanic IW field from wind (Alford et al., 2016). NI energy is deposited into the surface mixed-layer (ML), forcing NI currents that 'strum' IW modes; the relative rotation and propagation of these modes moves energy downward to the base of the thermocline, then into the interior (Zervakis & Levine, 1995). Generated NI IW propagate downward and equatorward into the ocean interior (Alford et al., 2016). For a flat-bottom basin bounded by the ocean surface, the vertical structure of IW modes exist as solutions to the Sturm-Liouville equation:

$$\frac{\partial^2}{\partial z^2}\eta(z) + \frac{N^2(z)}{c_n^2}\eta(z) = 0 \quad (4)$$

with boundary conditions $\eta(0) = \eta(D) = 0$, where D is the total water depth, η is surface displacement, n the mode number, and c_n the modal eigenspeed (Alford & Zhao, 2007). Low-modes tend to dominate NI IW energy and largely propagate laterally, while high-mode energy typically radiates downward (Alford et al., 2016). Seasonal NI mode amplitudes can be found using ML depth as a time-dependent step-function convolved with ML NI currents, as determined by a 'slab' model (discussed in Section 4). In general, the superposition of many modes forms an IW beam (Lamb, 2014). The downward propagation of IW energy is then defined by the dispersion relation:

$$c_{gz} = \frac{\omega^2 - f^2}{\omega m} \quad (5)$$

where m is the vertical wavenumber (Alford et al., 2012; Alford et al., 2013).

As IW and IT generated by sub-tidal, tidal, and NI processes propagate and impact irregular topography, they may break. Incident low-frequency IW energy cascades to the high-frequency IW continuum, and can result in the formation of strong along-slope currents and density overturns, ultimately resulting in mixing (Lamb, 2014). Breaking can occur due to a variety of processes; for example, shoaling IW can overturn, and barotropic tidal currents can generate breaking lee waves and hydraulic jumps over irregular topography (Lamb, 2014). Linear inviscid theory predicts that when downward propagating IW and IT impact a near-critical slope, the reflected wave amplitudes become infinite as group velocity and wave length approach zero, leading to instability (Lamb, 2014). Even when impacting non-critical slopes, incident IT can cause isopycnals to steepen and form unstable 'internal bores' which break and drive turbulent fluid up-slope (Martini et al., 2013). Whatever the mechanism, near-topography IW interactions energise the IW continuum, observations of which can be used to estimate elevated dissipation rates and mixing.

4 Barkley Canyon

The obtained Barkley Canyon horizontal velocity data are unique for both spatial and temporal consideration. Located at approximately 48.33°N 126.03°W, the Barkley Canyon region is about 75 km southwest of the coast of Vancouver Island, incising the continental slope and shelf (Figure 4). Barkley Canyon is a winding canyon up to 6 km wide and 13 km long, with an adjacent shelf-break region beginning around -150 m depth. Spread across the region, Acoustic Doppler Current Profilers (ADCP) provide current data for Ocean Networks Canada's (ONC) NEPTUNE cabled observatory. ADCP emit acoustic beams that triangulate Doppler shifts in the water column, providing directional velocity data time series through depth. The placement of ADCP across both continental slope and canyon topography allows for spatial analysis of coinciding IW events. Furthermore, ONC's Oceans 2.0 data portal offers publicly available processed data for each instrument, spanning over a decade. As such, the obtained datasets are substantially lengthy for IW research, allowing for typically difficult analysis of long-term variability.

The two ADCP for this study are located at the upper continental slope Upper Slope (Slope) and canyon-floor Axis sites (Figure 4). The Slope platform sits below the VICS shelf-break at a depth of -378 m (Figure 5), 15 km NW of Barkley Canyon, employing primarily 75 kHz ADCPs. The Axis platform is located at a narrow north-south channel on the floor of Barkley Canyon, about midway along its length at a sharp bend, and a depth of -968 m (Figure 5),

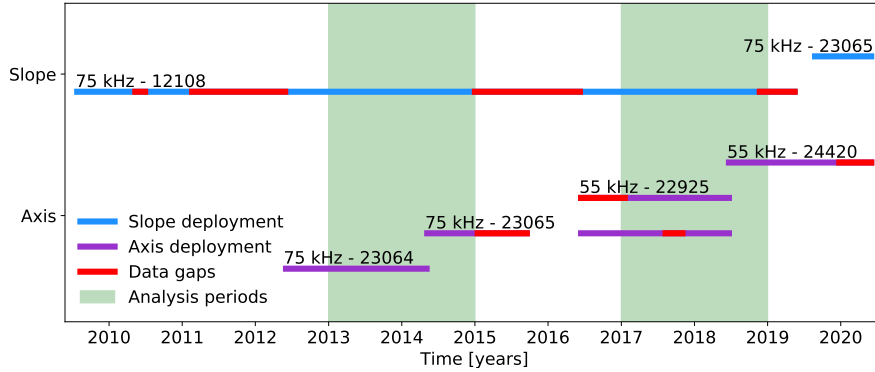


Figure 6. ADCP operating frequency, instrument ID, deployment periods, and data availability for the Slope and Axis sites. ONC operates and maintains regional instruments as part of the NEPTUNE cabled observatory. Due to maintenance and redeployment, years with comprehensive overlapping coverage (2013, 2014, 2017, and 2018) were selected for analysis.

employing both 75 and 55 kHz ADCPs. The 75 kHz Teledyne RDI Workhorse Long Ranger instruments were set to a vertical resolution of 8 m depth bins, and a continuous sampling rate of 2 seconds. The 55 kHz Nortek Signature55 instrument was set to a vertical resolution of 20 m depth bins, and a pulsed sampling rate of six 18-second pings followed by a 4.5-minute delay. For these sites, overlapping data coverage of good quality (e.g. minimal data gaps) is during 2013, 2014, 2017, and 2018 (Figure 6), due to ONC deployment and maintenance schedules.

An initial quality check of backscatter intensity and beam correlation was performed for the raw data (Figure 7), yielding quality thresholds of 65 and 115 counts, respectively. There is some seasonal variation in the vertical percent-good profiles based on these thresholds, notably in the fall, likely associated with seasonality of biological scatterers higher in the water column. Time-averaged profiles indicate regions of good data ($\geq 90\%$ good) below -50 m at Slope, and below -700 m at Axis. These depths avoids near-surface side-lobe contamination, and depth-dependent processing artifacts - non-physical high-frequency spikes in power spectra evident above about -600 m. For Axis instruments, with range well above the cut-off depth, up to -600 m is retained in plots for reference, and a line at -700 m indicates the upper extent of the analysis region.

Datasets were then acquired in 15-minute averaged sampling intervals for each analysis year, and combined and mapped to standard depth bins. Data gaps less than 25 hours were interpolated using a linear process. For large data

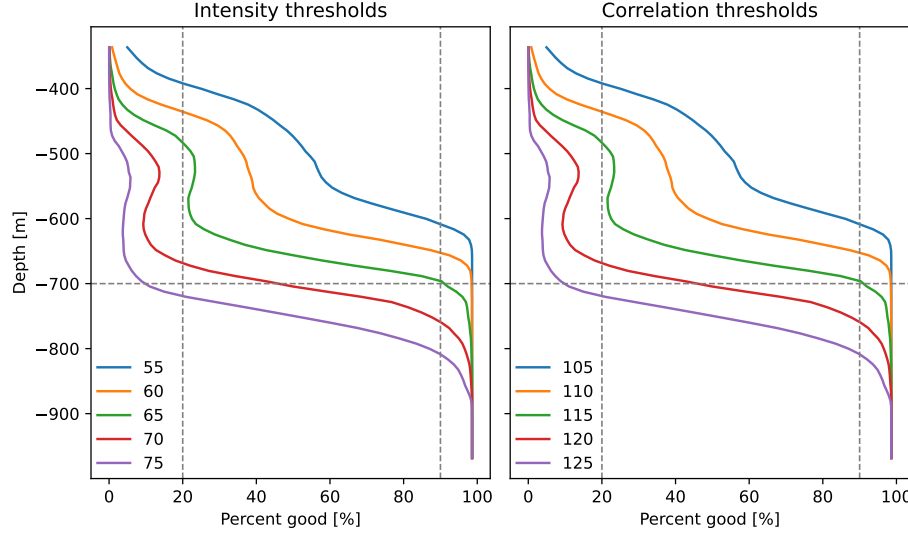


Figure 7. QA threshold profiles. Backscatter intensity and beam correlation percent-good vertical profiles for various thresholds. The green line in each was selected as the ideal threshold value due to the step-function-like steepness of the profile at 20 and 90%, in addition to the qualitative removal of depth-dependent processing artifacts and near-surface side-lobe contamination when used together as a screen.

gaps, annual datasets were combined using weighted averaging as necessary. All supplemental processing materials, including Python code and plots, are available in a project GitHub repository (Anstey, 2022).

At Slope, horizontal velocity data were rotated using a standard rotation matrix:

$$u_{rot} = u\cos(\theta) - v\sin(\theta) \quad (6)$$

$$v_{rot} = u\sin(\theta) + v\cos(\theta) \quad (7)$$

where θ is the rotation angle in radians. This better matches the physical cross-slope angle of approximately 30° ; u is referred to as cross-slope, and v as along-slope (Figure 4). At Axis, the along-canyon (v) direction is approximately north-south, so no rotation was necessary; u is 'cross-canyon'.

To account for depth-dependent stratification, horizontal velocity data were WKB-scaled as:

$$u_{WKB}(z) = u(z) \sqrt{\frac{N_0}{N(z)}} \quad (8)$$

and for energy density as:

$$\phi_{WKB}(z) = \phi(z) \frac{N_0}{N(z)} \quad (9)$$

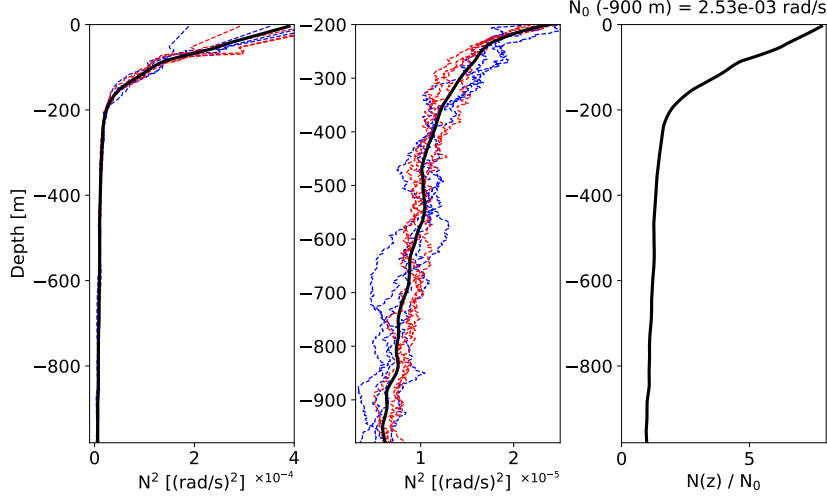


Figure 8. N^2 parameter and WKB scaling factor. Buoyancy results were smoothed and averaged for the four analysis years at La Perouse station LB14 CTD data, and are displayed through the water column (left) and below -200 m (centre). Casts were taken in May (blue) and September (red). A WKB scaling factor (right) was determined for use in Equation 9, based on N_0 averaged around -900 m.

with a reference buoyancy frequency of $N_0 = 2.53 \times 10^{-3} \text{ rad/s}$ averaged around -900 m (Althaus et al., 2003). Buoyancy data were determined from climatology data obtained from the nearby (20 km S) station LB14. Data were sampled annually in May and September, during Fisheries and Oceans Canada (DFO) La Perouse cruises, casting down to -1180 m. Depth profiles were obtained for temperature, pressure, and salinity, $S(z)$, to find potential density, $\rho_\theta(z)$, following the UNESCO EOS 80 polynomial (Mamayev et al., 1991). Depth-dependent buoyancy was then determined as in Equation 1 (Figure 8). There is little inter-annual variability in the buoyancy depth profiles.

Component-wise power spectral density (PSD) was determined from the WKB-scaled horizontal velocity data for each depth bin, using a Welch spectrogram process with a Hanning window of 256 data-points (~ 2.7 days), 50% overlap, and detrended in time to avoid a 0 Hz offset. Short 1.3 day and long 5.3 day spectra were also computed. The noise floor of each instrument was determined from the standard error of the mean relative to instrument sampling intervals and uncertainties from Nortek and RDI. 95% confidence intervals were determined using a chi-squared method.

For rotational dependence, rotary power spectra were determined as for PSD, though using a modified spectrogram process based on the work of Gonella (1972) and Thomson and Emery (2014). To summarise, the adjustment to find

the counter-clockwise (CCW) and clockwise (CW) components of a complex horizontal velocity vector, $\mathbf{w}(t) = u(t) + iv(t)$, is the addition or subtraction of twice its quadrature spectrum, Q_{uv} , as:

$$\text{CCW} = \frac{1}{2}[S_{uu} + S_{vv} + 2Q_{uv}] \quad (10)$$

$$\text{CW} = \frac{1}{2}[S_{uu} + S_{vv} - 2Q_{uv}] \quad (11)$$

where S_{uu} and S_{vv} are the typical complex autospectra used for PSD (Thomson & Emery, 2014). In general, a stronger CW component indicates downward propagation of energy, and vice-versa.

The open-ocean GM IW spectrum was determined using local parameters for $f = 1.73 \times 10^{-5}$ Hz, $g = 9.81(m/s)^2$, and N_0 , along with canonical values for the surface-extrapolated buoyancy frequency ($N_{GM} = 5.24 \times 10^{-3}$ rad/s), e-folding scale of $N(z)$ (1.3×10^3 m), mode scale number $j* = 3$, and dimensionless IW energy parameter $E = 6.3 \times 10^{-5}$, as in Munk and Wunsch (1998). The directional GM spectrum was adapted to rotary form through application of the rotary consistency relation, as described in Section 3 (Levine, 2002; Polzin & Lvov, 2011).

For wind forcing of NI IW, a slab model was conducted as in D'Asaro (1995) and Alford (2001), providing a simplified idea of the ML response to NI wind forcing (Alford et al., 2016). Though simple, the model is continuously being improved to better account for non-homogeneous internal ML processes, and ML to pycnocline energy transfer (Alford & Zhao, 2007; Jarosz et al., 2007; Alford et al., 2016; Zheng et al., 2017; Voelker et al., 2020; Alford, 2020). From surface wind time series, wind stress is calculated as in Garratt (1977):

$$\tau_0 = \rho C_D V(z)^2 \quad (12)$$

where ρ is the density of air (approximated as 1), $V(z)$ is the complex wind velocity vector, and C_D is the characteristic drag coefficient determined by:

$$C_D \times 10^3 = 0.51V^{0.46} \quad (13)$$

For appropriate seasonally, a ML of seasonally varying depth, H , must be considered. Assuming a null initialisation parameter u_{I1} at time t_1 , wind generated slab layer currents at time t_2 are then computed as:

$$u_{I2} = u_{I1}e^{-\omega\Delta t} - \frac{T_t}{H\omega^2}(1 - e^{-\omega\Delta t}) \quad (14)$$

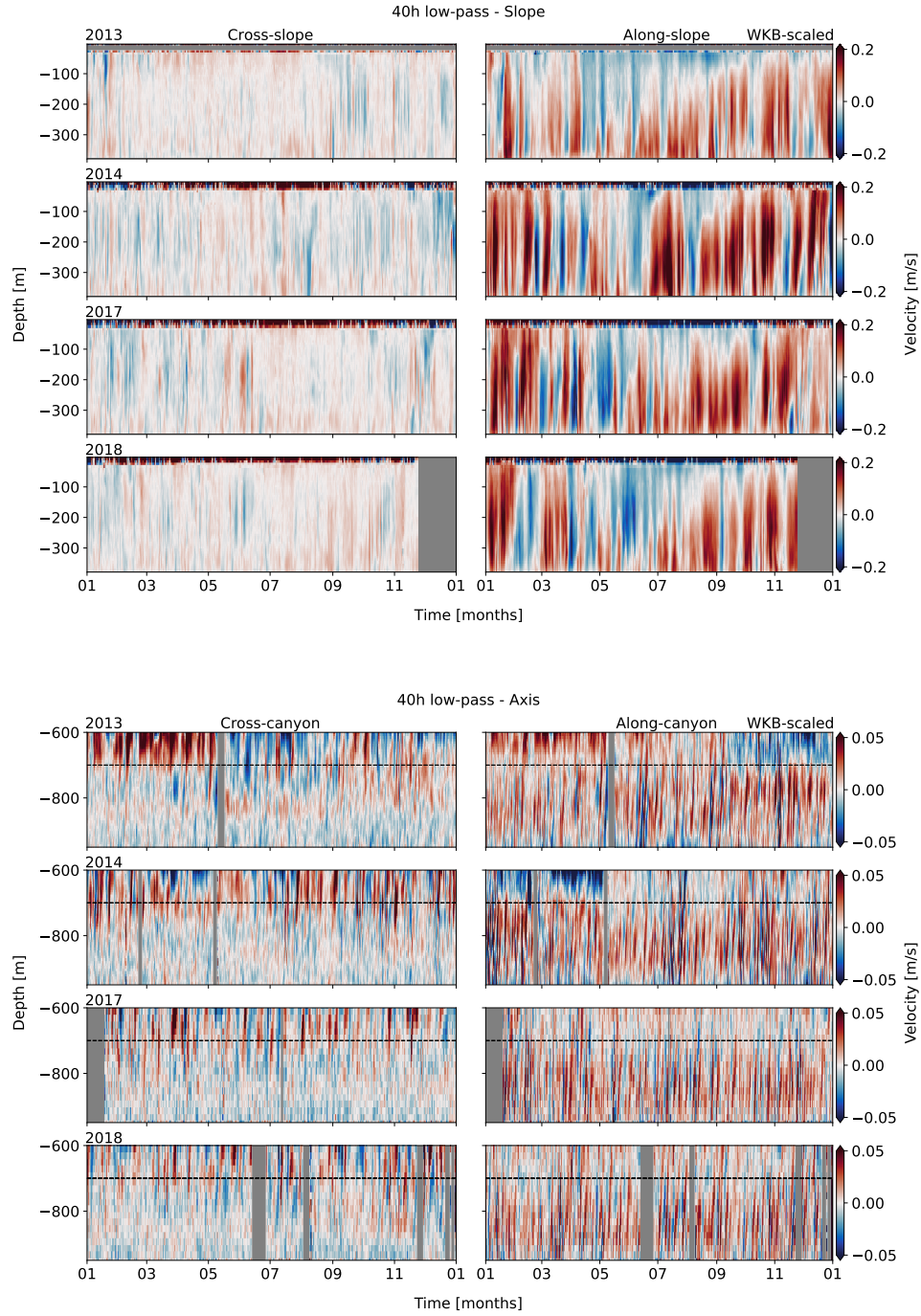


Figure 9. 40-hour low-pass WKB-scaled horizontal velocity data for Slope (top) and Axis (bottom). Components are separated as cross- (left) and along-slope/canyon (right). At Axis, the dashed line is the upper limit of the analysis depths (-650 m). There is a clear seasonal cycle in the along-slope component at Slope, while seasonality is less apparent in the predominantly along-canyon flow at Axis.

where a damped rotation frequency, ω , is determined as:

$$\omega = r + if \quad (15)$$

with $r = 0.15f$ as an artificial damping parameter, as defined in Alford (2001); and

$$T_t = \frac{\Delta T}{\Delta t} \quad (16)$$

is related to the complex stress vector, defined as:

$$T = \frac{\tau_x + i\tau_y}{\rho_{ML}} \quad (17)$$

where $\rho_{ML} = 1024 \text{ kg/m}^3$ is the average density of the ML. The slab currents are then band-passed for their NI component, u_{NI} .

5 Results

5.1 Observations

5.1.1 Mean currents

Regional low-frequency mean currents are inter-annually consistent, topographically guided, and seasonally site-dependent (Figure 9). To identify long-term mean currents, a 40-hour, 8th-order, digital low-pass Butterworth filter was applied to the WKB-scaled horizontal velocity data. There is little inter-annual variability in mean currents, though each site has unique seasonality. At Slope, mean currents below -50 m are as expected for this portion of the California current system (Figure 9): generally poleward along-slope (up to $> 0.2 \text{ m/s}$) through depth, with a quick transition to upwelling-favourable equatorward flow in the late-spring (April/May), with the deep poleward currents shoaling by fall (Thomson & Krassovski, 2015). In the canyon, mean currents below -700 m are consistently up-canyon (up to $> 0.05 \text{ m/s}$), with down-canyon flow $< 50 \text{ m AB}$ (Figure 10). A two-week rolling depth-average between -700 and -900 m yields consistently positive (up-canyon) velocities up to 0.02 m/s , with annual means of $0.007 - 0.010 \text{ m/s}$. Two-month snapshots show the up-canyon flow is comprised of shoaling pulses with periodicity of about a week (Figure 9b). Shoaling is consistent seasonally and inter-annually (not shown).

5.1.2 High frequency currents

High-frequency ($< 40\text{-hour}$) velocity data show variable periodicity and vertical structure. Subtracting the 40-hour low-pass currents from the total yields residual high-frequency currents - flows with periodicity less than 40-hours

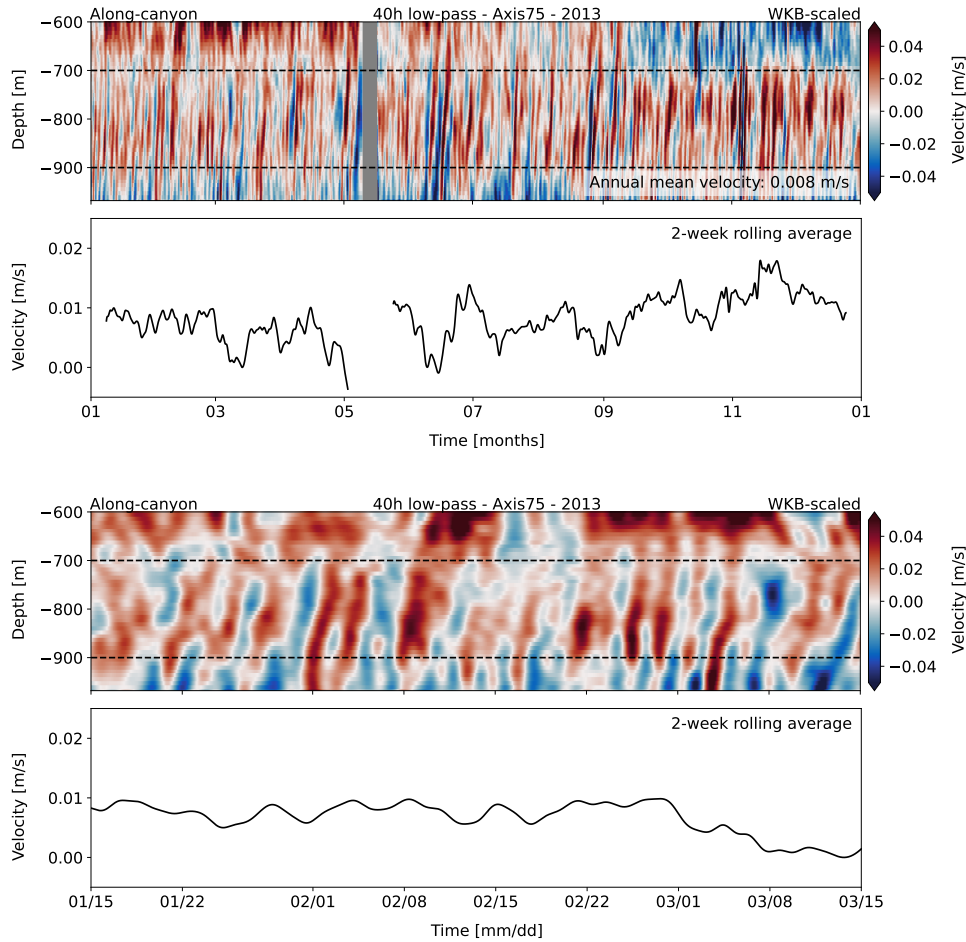


Figure 10. 40-hour low-pass WKB-scaled horizontal velocity data showing along-canyon mean currents for Axis, annually (top) and in a two-month snapshot (bottom). Mean up-canyon flow is within the dashed lines; a thin near-bottom layer of mean down-canyon flow is below.

(Figure 11). A two-week snapshot during the annually recurring April/May mean current transition reveals the presence of tidal and NI IW with non-uniform vertical structure. At the Slope site, high frequency currents reach over 0.1 m/s in both cross- and along-slope directions, and there is periodic shoaling above -250 m depth (about 150 m AB). At Axis, high-pass currents are strongest below -750 m (about 250 m AB), up to about 0.2 m/s and mostly along-canyon, with increased non-uniformity in the vertical structure above.

Annual mid-depth (-195 m and -800 m) power spectra of the high frequency currents at each site show strong tidal and NI influence (Figure 12), with site- and frequency-dependent topographic guiding. Inter-annual variability is

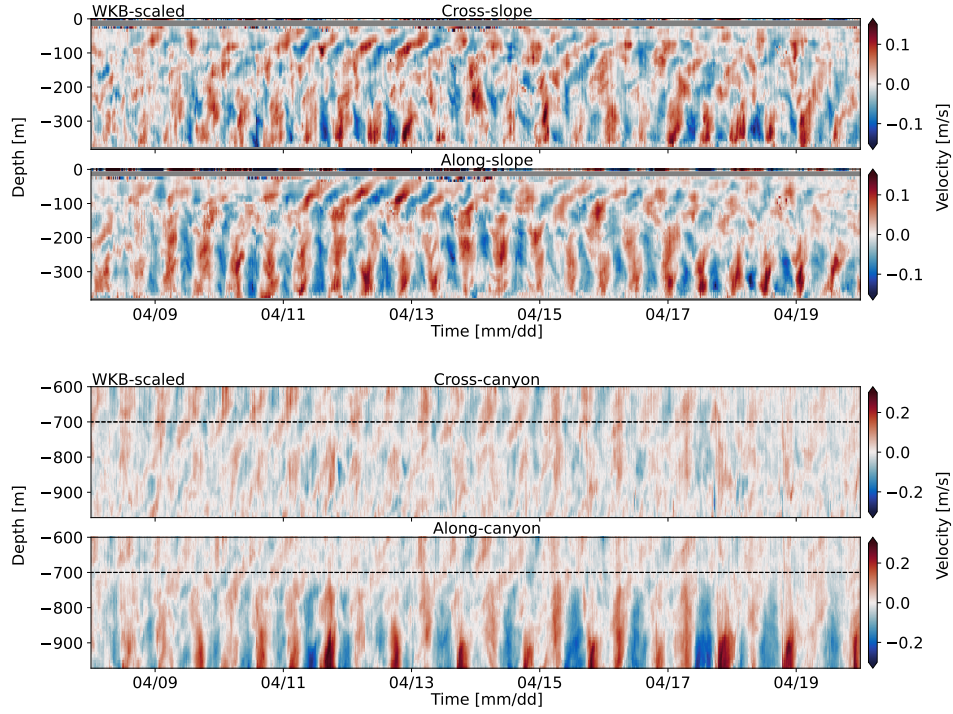


Figure 11. 40-hour high frequency WKB-scaled horizontal velocity data for Slope (top) and Axis (bottom), in April 2013. Components are separated as cross- (upper) and along-slope/canyon (lower). There are IW and IT of varied frequency, non-uniform vertical structure, and depth-dependence.

minimal (each line of the same colour is a different year), with annual spectra overlapping within the 95% confidence interval. The low-frequency sub-diurnal broadband ranges up to 1.00×10^{-5} Hz. The most defined spectral peaks are of the diurnal (1.16×10^{-5} Hz), NI (1.73×10^{-5} Hz), and semidiurnal (2.24×10^{-5} Hz) frequencies. Closely associated tidal constituents (such as S_2 and M_2) were identified in high frequency-resolution spectra (not shown) as having similar topographic and seasonal responses, and so are not resolved due to spectral averaging for ease of analysis; tidal constituents are therefore referred to generally (e.g. diurnal). The high-frequency IW continuum band ($7.00 \times 10^{-5} - 1.20 \times 10^{-4}$ Hz) ranges between M_6 ($\sim 6.8 \times 10^{-5}$ Hz) and the near- N spectral shoulder ($2.00 \times 10^{-4} - 1.00 \times 10^{-3}$ Hz).

At Slope, the sub-diurnal broadband is almost entirely along-slope (an energy ratio of up to 10:1, compared to cross-slope), with strength increasing inversely to frequency; the diurnal constituent is strongest cross-slope (over 3:1); the NI peak is equally distributed (1:1); and, the semidiurnal constituent is strongest along-slope (up to 2:1). The continuum is slightly stronger cross-slope, and

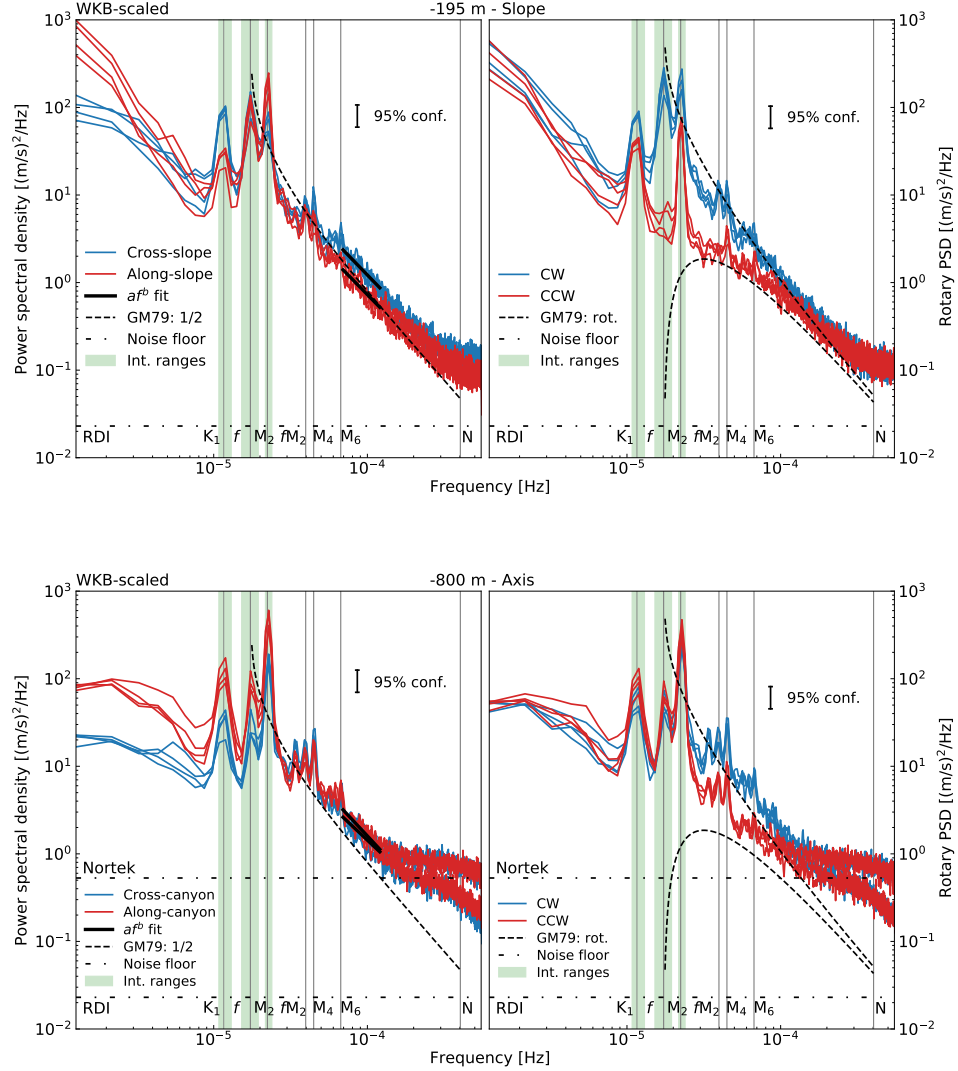


Figure 12. Mid-depth annual PSD (left) and rotary (right) spectra of WKB-scaled horizontal velocity data, for Slope (top) and Axis (bottom). Each line of the same colour is a different year. For PSD, cross- (blue) and along-slope/canyon (red) components are shown; for rotary, CW (blue) and CCW (red) components are shown. 95% confidence intervals are indicated by the black bar. Instrument noise floors (dotted line) and primary frequency constituents with integration range (vertical lines and green shading) are shown. For PSD, black lines indicate continuum power-law fit, and the dashed line is the GM79 spectrum (1/2 amplitude). For rotary, the GM79 spectrum is in rotary components (CW upper). Spectra at both sites are characteristically red, with prominent tidal and NI peaks.

trails off slightly whiter than the expected open-ocean GM slope of -2 (discussed in Section 5.2.5). Near N , a spectral shoulder is partially resolved as

a whitening effect, and is better observed in the raw (2-second) spectra (not shown), discussed in Section 5.2.6. All bands are stronger in the CW rotary component.

At Axis, compared to Slope, power is weaker at low frequencies below 4.00×10^{-6} Hz. Sub-tidal, tidal, and NI bands are all trend towards along-canyon (from 3:1 at sub-diurnal, to 2:1 at semidiurnal, compared to cross-canyon), rectilinear motions. Above the semidiurnal peak, the super-tidal and continuum ranges are mostly CW (about 2:1), becoming rectilinear again approaching the near- N spectral shoulder. The near- N spectral shoulder is more pronounced at Axis in 2013 and 2014, seen below the Nortek 55 kHz noise floor which masks the effect in 2017 and 2018 (discussed in Section 5.2.6).

5.1.3 Depth dependence

At each site, there is adjustment of spectral power near topography that is frequency-dependent. The WKB-scaled PSD and rotary spectra were time-averaged for annual 2D depth-frequency analysis (Figure 13). Results show a general increase (or decrease, for NI at Slope) in spectral power (over an order of magnitude) in a concentrated layer < a few hundred metres above bottom (AB).

At Slope (Figure 13a), the sub-diurnal, tidal, and continuum bands show near-slope intensification of IW energy. In contrast, the NI band is attenuated near the slope, below an average depth of -250 m (130 m AB). Near-slope adjustment is up to a factor of 10, compared to background energy. For the broadband sub-diurnal range, intensification is mostly along-slope and CW. The diurnal intensification is mostly along-slope and CCW. The NI near-slope attenuation is entirely CW. The semidiurnal intensification is mostly along-slope and strongly CW. Continuum intensification is mostly cross-slope and CW.

At Axis (Figure 13b), most constituents show rectilinear, along-canyon near-bottom intensification, below an average depth of -750 m depth (230 m AB). Near-bottom adjustment is up to a factor of 100, compared to background energy. The sub-diurnal, diurnal, and NI intensification is entirely along-canyon, with little to no power in the cross-canyon direction. The NI band, in contrast to Slope, has bottom-intensified flow that is almost entirely along-canyon. The semidiurnal intensification is strongly along-canyon, but with a medium-strength cross-canyon signal that is sharply attenuated below -900 m. Continuum strength varies between cross- and along-canyon, and is mostly CW.

A vertical scale analysis roughly agrees with the qualitative observations of

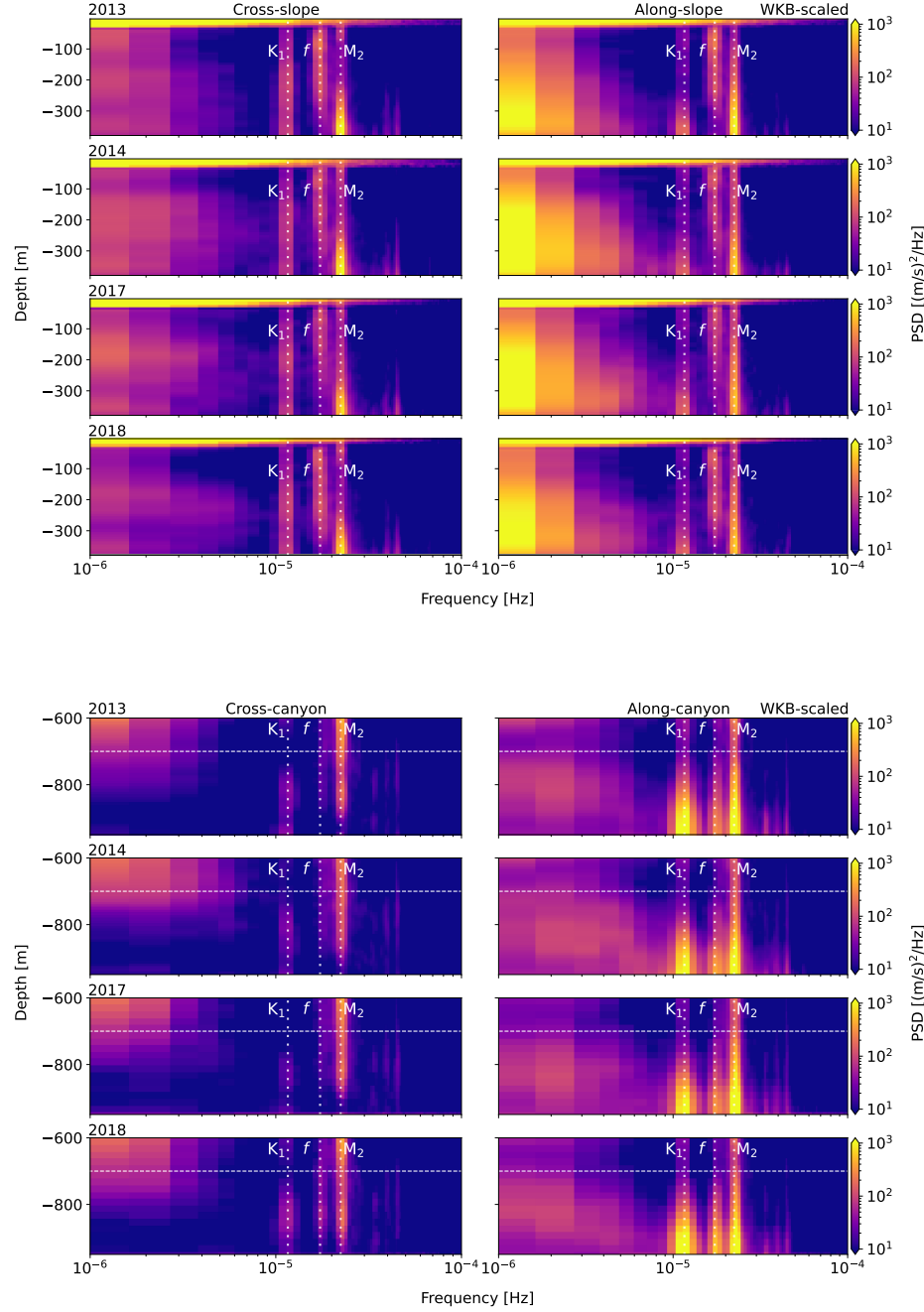


Figure 13. Depth-frequency PSD for Slope (top) and Axis (bottom). Components are separated as cross- (left) and along-slope/canyon (right). Determined from WKB-scaled horizontal velocity data. There is near-bottom intensification of individual frequency constituents (and near-bottom attenuation of the NI band, at Slope).

enhanced layer thickness. Gemmrich and Klymak (2015) found that mode-1 IW incident on sloped topography can induce a near-bottom turbulent flow layer, and that the vertical scale of the effect can be approximated as:

$$H \approx \frac{\pi U}{N} \quad (18)$$

where U is the forcing by horizontal velocity. For strong near-bottom velocities (Figure 11) and approximate buoyancy values (Figure 8) for near-topography depths at Slope ($U \approx 0.15$ m/s; $N \approx 3.5 \times 10^{-3}$ rad/s, at -350 m) and Axis ($U \approx 0.25$ m/s; $N \approx 2.5 \times 10^{-3}$ rad/s, at -900 m), estimates yield vertical scales of 135 m and 314 m, respectively. Results are similar to the qualitative thickness of 130 m AB at Slope, somewhat greater than the observed 230 m AB at Axis, and agree with the results of Gemmrich and Klymak (2015) for similar forcing and stratification. It should be noted that the CTD climatology data are from a nearby open-ocean site, and so do not reflect changes in stratification near topography.

5.2 Frequency-dependent response

There is frequency-dependent variability in the seasonality of the near-topography enhancement layer (and attenuation for NI at Slope). Little inter-annual variability is observed, noted only in the more intermittent sub-diurnal and NI seasonality. WKB-scaled PSD and rotary spectra were integrated over bandwidths comprising each constituent's peak or frequency range (shown as shaded green in Figure 12), for each depth bin, yielding 2D estimates of depth-band power. Constituent frequency ranges are sub-diurnal ($\leq 1.08 \times 10^{-5}$ Hz), diurnal ($1.08 - 1.30 \times 10^{-5}$ Hz), NI ($1.52 - 1.95 \times 10^{-5}$ Hz), semidiurnal ($2.17 - 2.39 \times 10^{-5}$ Hz), continuum ($7.00 \times 10^{-5} - 1.20 \times 10^{-4}$ Hz), and shoulder ($2.00 \times 10^{-4} - 1.00 \times 10^{-3}$ Hz).

5.2.1 Sub-diurnal

At Slope, sub-diurnal ($\leq 1.08 \times 10^{-5}$ Hz) enhancement layer seasonality consists of intermittent pulses, strongest in fall and winter, and is one of few observations that is not inter-annually consistent (Figure 14a). At Axis, seasonality is weak, showing an occasional fall or winter pulse (Figure 14b). Seasonal forcing of the sub-diurnal constituent is inconclusive, as there is no correlation with wind, tides, or the expected low-frequency along-slope mean currents (Figure 9). Low-frequency flows can be affected by a variety of physical processes near slope, shelf, and canyon topography (Cummins, 2000), and a forcing analysis for the sub-diurnal range is left for further study.

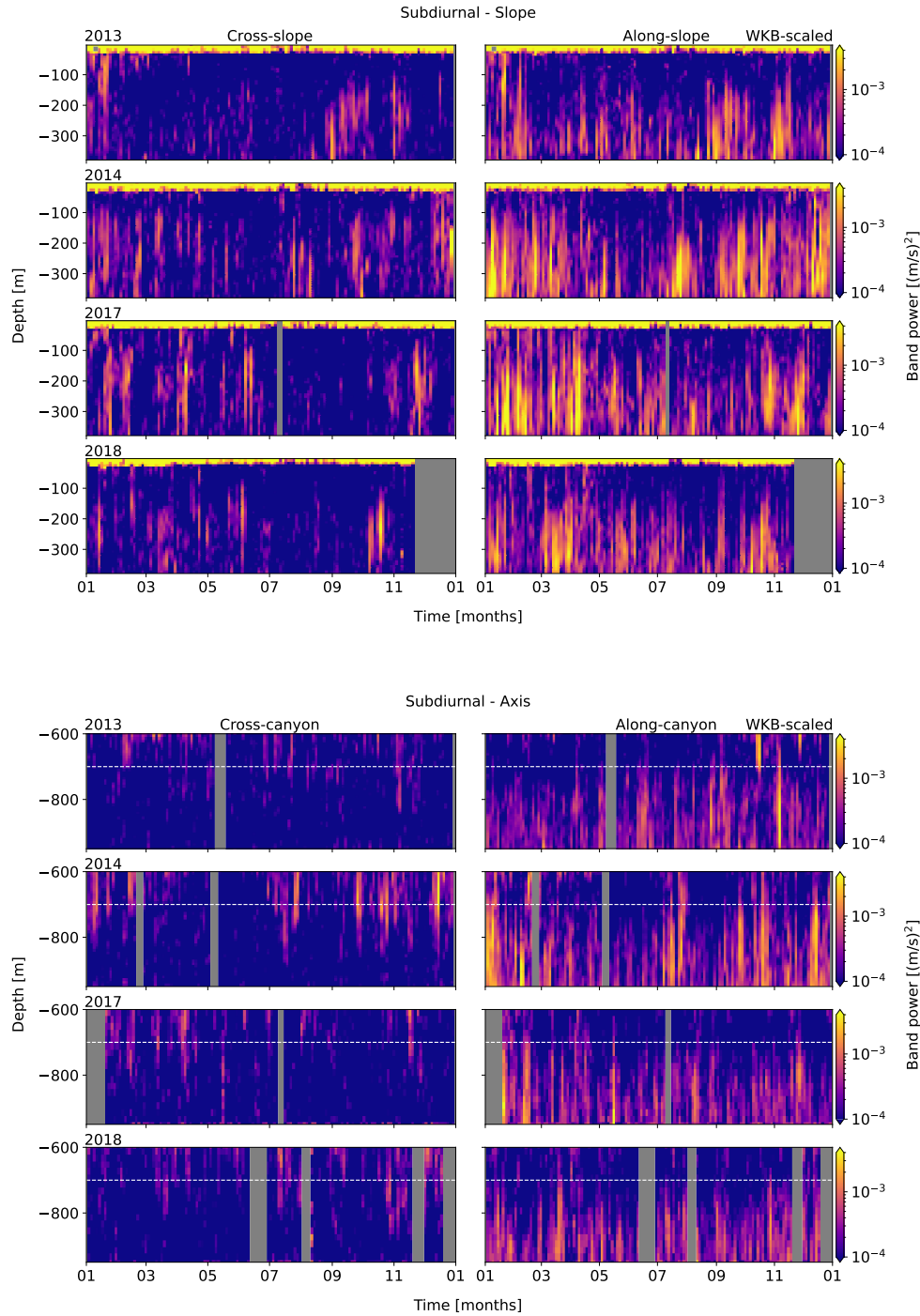


Figure 14. Band-integrated sub-diurnal PSD for Slope (upper) and Axis (lower), from WKB-scaled horizontal velocity data. Cross- (left) and along-slope/canyon (right) components are shown. Each row represents an analysis year, labelled at upper-left.

5.2.2 Diurnal

Diurnal ($1.08 - 1.30 \times 10^{-5}$ Hz) enhancement seasonality at Slope (Figure 15a) is inter-annually consistent, with energy elevated late-spring through summer (months 5-8) and again (weaker) in the fall/early-winter (months 11-1). Seasonality at Axis is not readily apparent (Figure 15b).

The diurnal band is in sync with the local barotropic spring-neap cycle, fortnightly and seasonally, at both sites (Figure 16). Surface-level data were obtained from the Canadian Hydrographic Service (CHS) operated gauge in Tofino, approximately 90 km due north of Barkley Canyon, as hourly time-series of deviation from chart datum, with power spectra diurnally band-passed using the same process as for observations. Comparing long-term seasonality, the Tofino barotropic spring-neap amplitudes peak in months 6-8 and 11-2, corresponding well with the diurnal observations, and consistent inter-annually. Fortnightly, 3-month phase-lag correlations were performed between the depth-mean diurnal power and nearby surface level time series, for months 1-3, 4-6, 7-9, and 10-12, each year. Phase-lag correlations range from 0 to 1 day at Slope (inter-annual average of 0.5 days), and 0 to 2 days at Axis (inter-annual average of 1.1 days) - both less than the time-resolution of the spectral estimates (~ 2.7 days) used for correlations. It should be noted that Axis estimates are only partial-depth and cannot fully resolve barotropic water-column motions, potentially contributing to observed phase offsets. Regardless, the diurnal observations are largely in sync with both the fortnightly and seasonal local barotropic spring-neap cycle.

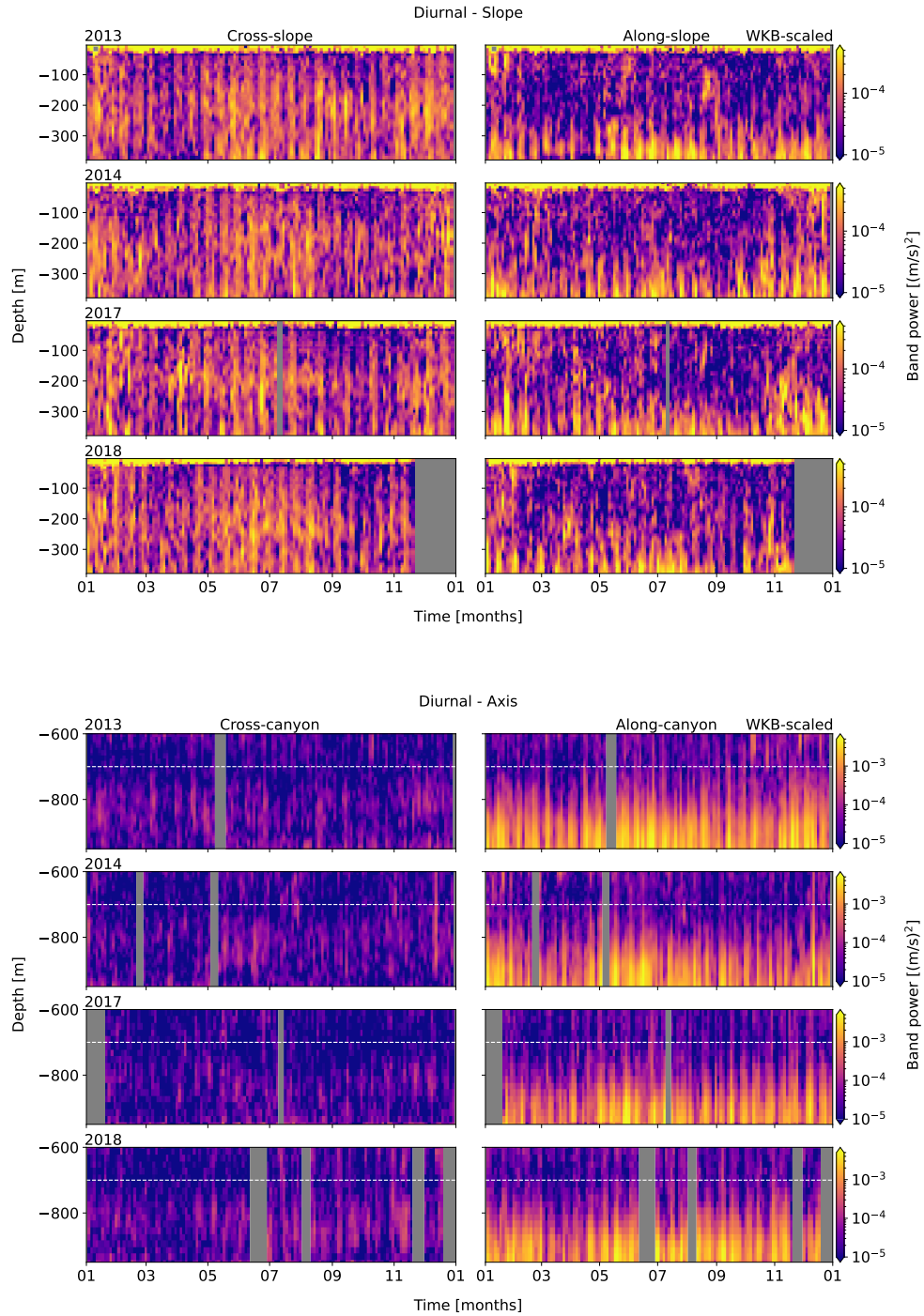


Figure 15. Band-integrated diurnal PSD for Slope (upper) and Axis (lower), from WKB-scaled horizontal velocity data. Cross- (left) and along-slope/canyon (right) components are shown. Each row represents an analysis year, labelled at upper-left.

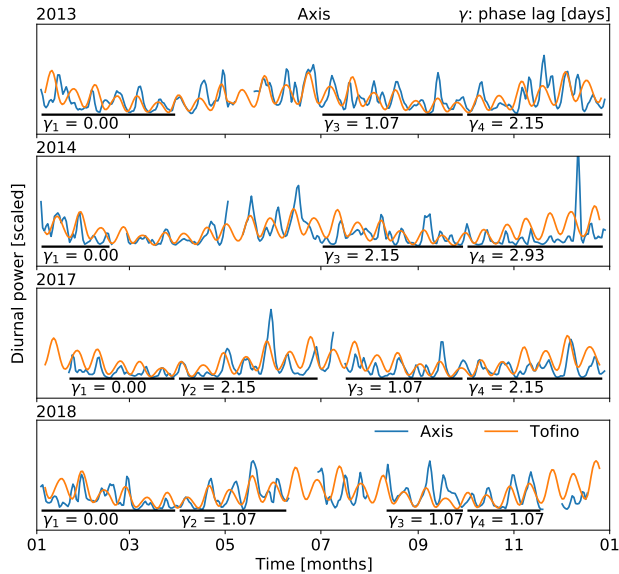
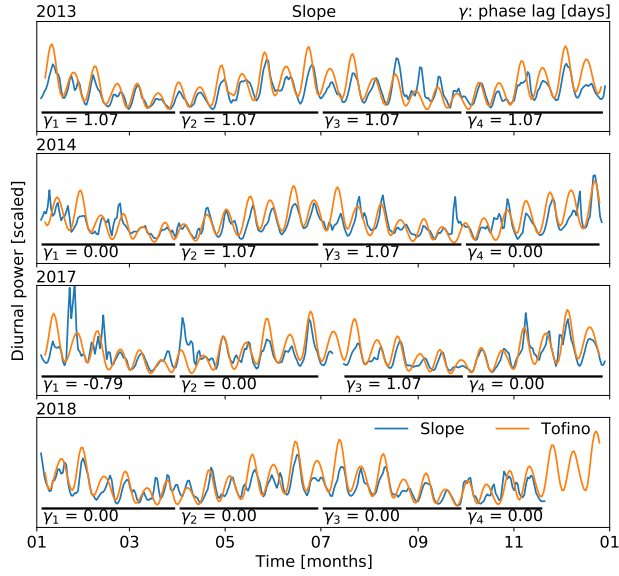


Figure 16. Diurnal barotropic forcing comparison. Phase-lag correlation and amplitude (scaled) comparisons for band-integrated power of diurnal surface level data (Tofino, orange) and WKB-scaled depth-mean diurnal power (blue) at Slope (top) and Axis (bottom). Black bars indicate seasonal correlation ranges. There is a consistent yet minor phase-lag, less than the time-scale of each spectral estimate.

5.2.3 Near-inertial

At Slope, NI ($1.52 - 1.95 \times 10^{-5}$ Hz) seasonality above the attenuation region is highly intermittent, with pulses occurring most likely in the fall and early-winter, though possible year-round (Figure 17a). At Axis, generally only significant fall and early-winter events from Slope are evident (Figure 17b). Seasonality is inter-annually consistent, but specific events are not.

For prominent pulses at Slope, there are periods of downward propagation of NI energy from the ML (above -50 m) to about -100 m, lasting up two weeks, after which the deep response increases quickly. At Axis, the timing of observed pulses appears to correspond to the delayed deep response at Slope. Figure 18a shows a sample event in September, 2014. An event (likely wind, to be discussed), deposits energy into the ML on September 3. Over the next 8 days, energy is transferred down to about -100 m. Upon reaching this depth, there is an immediate deep response. Energy continues to pool around -100 m, maintaining the deep response until September 14, when NI energy appears to have dissipated. There are many of these events each year, enumerated in Figure 19b. The fall sees the most events, all of which are short lived, from 7-9 days, while the winter has the longest events, up to 16-18 days.

Slab model results indicate NI forcing is qualitatively linked with regional wind events in the fall and early-winter (Figure 20). Wind data were obtained from the closest Fisheries and Oceans Canada (DFO) weather buoy, La Perouse (46206, 50 km N), as time series of magnitude and direction. Regional seasonally varying ML depth, H , is defined by Thomson and Fine (2003) and Li et al. (2005) for nearby (35 km NW) Line P Station 3; the ML is thick in winter and spring (down to about -60 m), and thinnest summer through early-fall (up to about -20 m). There are large wind data gaps during later years (2014, 2017, and 2018), so 2013 is used as the sample year. Results for later years are available in Appendix A (Section 8). Results yield time series of NI ML currents exceeding 0.1 m/s that are qualitatively similar to wind data, most notably in the fall and early-winter. However, not every event that shows up in the ML is evident in the NI depth-band observations.

Seasonal slab model correlations with NI depth-band power suggest interior NI response to wind forcing is strongest in summer and fall (not shown). To better quantify wind forcing of NI depth-band power, seasonal correlations were obtained similarly to diurnal spring-neap forcing. Correlation estimates were initially poor; the apparent delay in the deep response may affect correlation with the quicker slab response. To cope, a 2-month rolling average was applied to each time-series and relaxed until correlations began to devolve. Ideal rolling average intervals were found to be 3-weeks for the slab

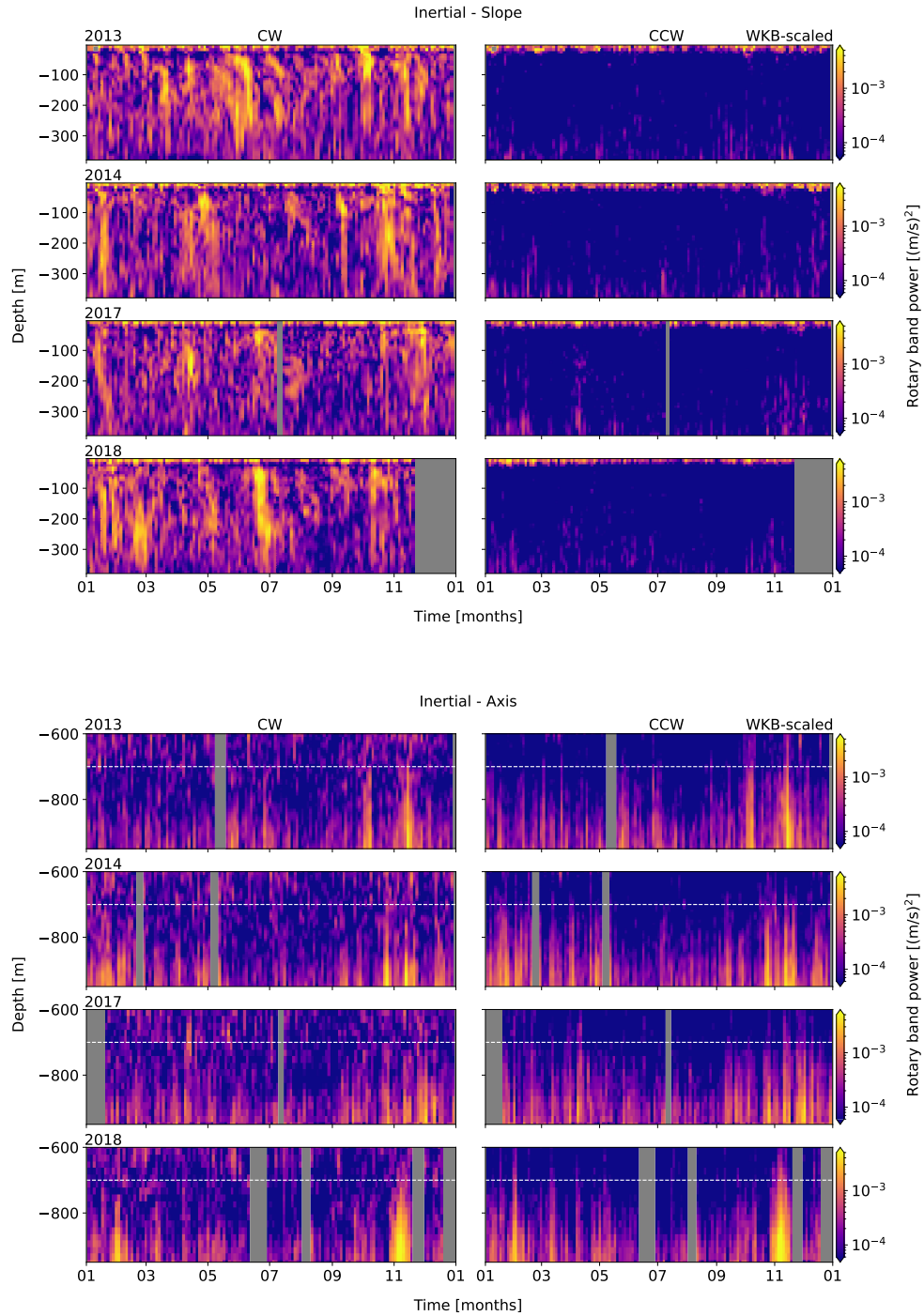


Figure 17. Band-integrated NI rotary PSD for Slope (upper) and Axis (lower), from WKB-scaled horizontal velocity data. CW (left) and CCW (right) components are shown. Each row represents an analysis year, labelled at upper-left.

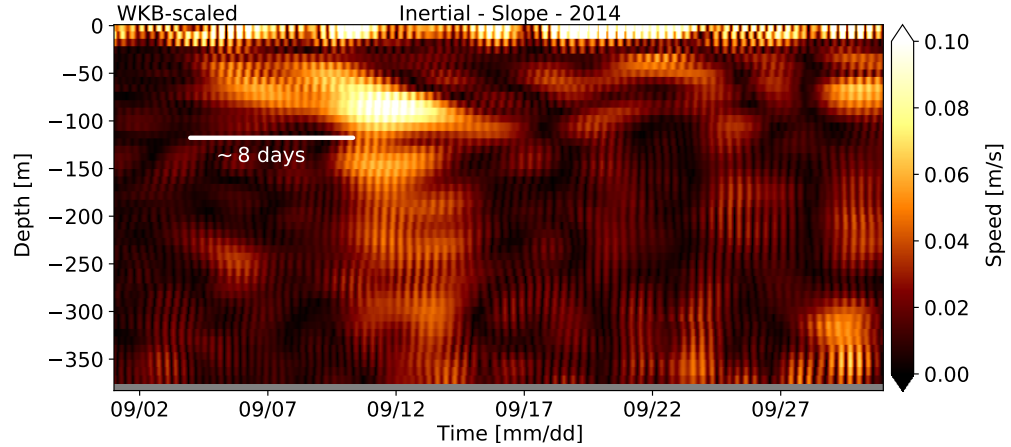


Figure 18. Transfer of NI energy in band-passed NI velocity (total) for September, 2014. A wind event excites NI energy in the ML around September 9. Energy is transferred down to about -100 m over about 8 days, after which there is a deep response.

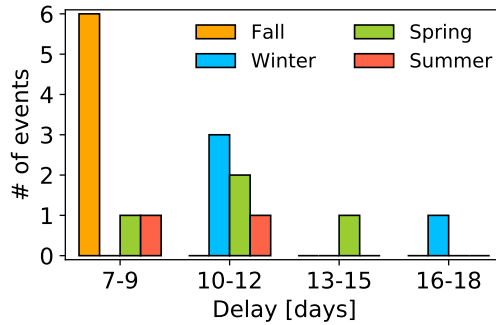


Figure 19. Histogram of delayed NI events. Delayed NI deep response events are most common and short-lived in the fall, least common in summer, and longest in the winter.

data, and 1-week for site observations, as the wind data were more highly variable to begin (not shown). At Slope, correlations are strong-positive in the fall, and weak- to medium-positive in summer. At Axis, correlations are strong-positive in summer, and weak- to medium-positive in fall. Seasonal correlations are otherwise inconsistent. The fall and summer correlation periods encompass notable wind events that occur while the ML is thin, and there is a more notable deep response.

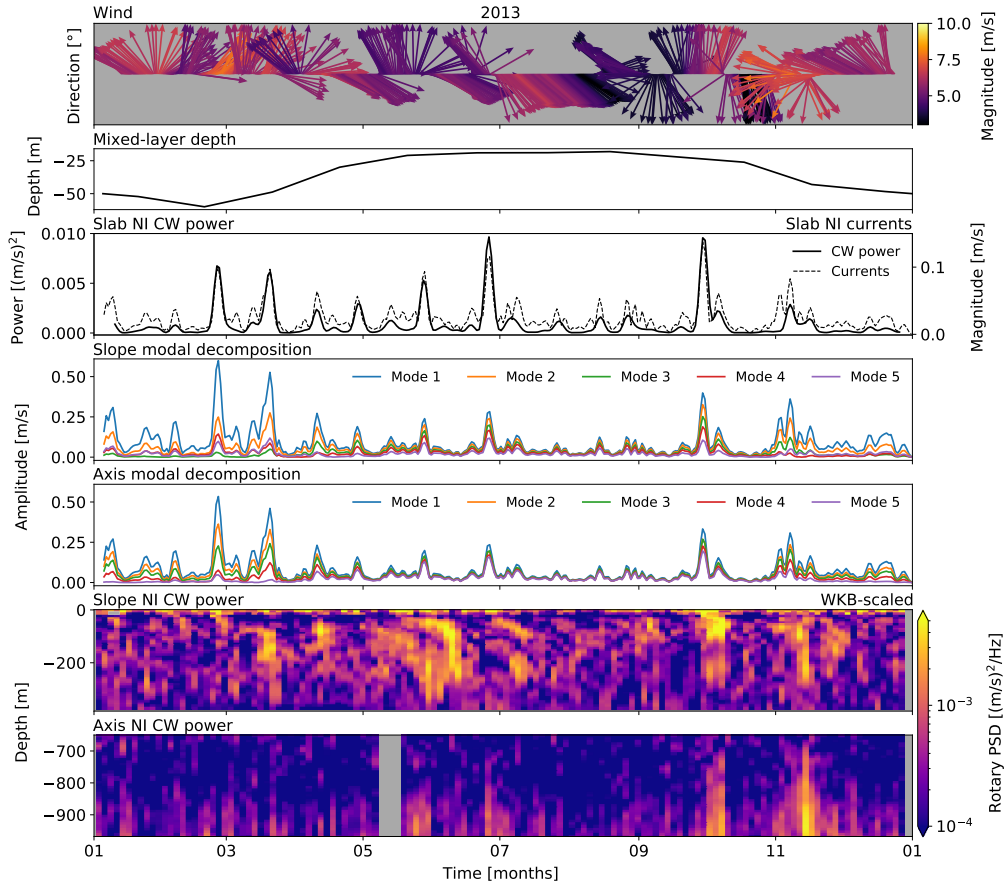


Figure 20. NI forcing analysis for 2013. Panels are (i) wind direction and amplitude, (ii) monthly-averaged ML depth for Line P station 3 as determined by Li et al. (2005), (iii) slab model NI CW power and NI currents, (iv, v) seasonal mode amplitudes for Slope and Axis, and (vi, vii) band-integrated NI CW power at Slope and Axis. There appears to be a complex relationship between the wind, ML, slab currents, and mode amplitudes in driving the NI observations, with the most obvious effects in the fall. Due to significant data gaps, plots for other analysis years are in Appendix A (8).

Seasonal vertical mode amplitudes suggest high-mode contributions lead to greater NI deep response (Figure 21). For NI IW generation by the NI ML currents, the stratification-dependent vertical mode structure is determined as described in Section 3. When the ML is thin, contributions from low modes (1 and 2) and high modes (3, 4, 5) are about equal ($\sim 52\%$ low modes); when the ML is thick, modes 1 and 2 dominate ($\sim 74\%$). Similar to the slab correlations, there is a greater deep response when the ML is thin and higher modes are equal contributors, such as in the early-fall when strong storms begin to arrive.

High modes contribute most in the summer when the ML is thinnest, though there are few storms this time of year; however, even weak summer wind events occasionally warrant a deep response. In contrast, there are many strong wind events in winter and spring when the ML is thick and low modes dominate, but there is often little or no deep response. A deep response associated with high-mode NI IW is not unexpected, though is somewhat misunderstood (Gill, 1984; Zervakis & Levine, 1995; Alford, 2003); though low-modes tend to dominate NI IW energy they largely propagate laterally, while high-mode energy radiates downward and equatorward (Alford et al., 2016).

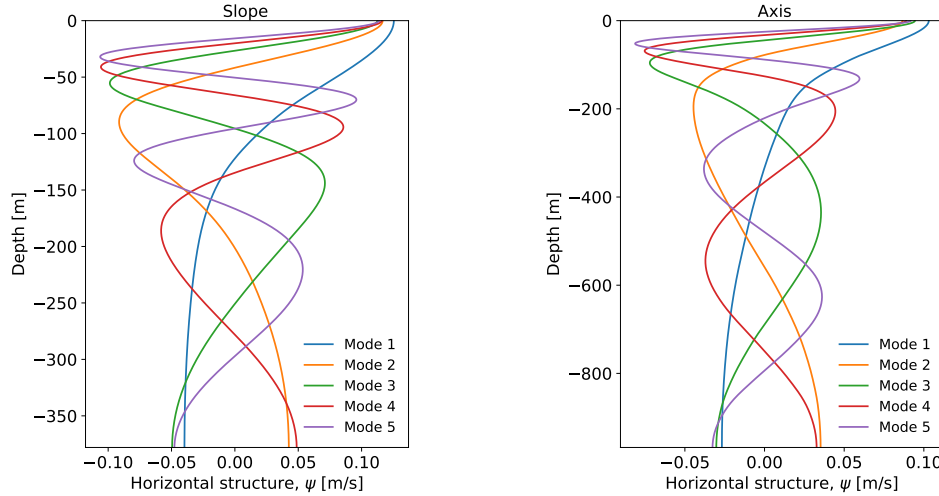


Figure 21. Vertical mode decomposition. Depth-dependent horizontal structure of mode amplitudes, for Slope (left) and Axis (right). Mode structure is dependent on site depth and the local stratification profile.

5.2.4 Semidiurnal

Semidiurnal ($2.17 - 2.39 \times 10^{-5}$ Hz) enhancement layer seasonality at Slope is inter-annually consistent and subtle, showing a slight pulse that begins in the late-spring/early-summer (months 4/5) and an even weaker pulse in the fall/early-winter (Figure 22a). Seasonality at Axis is not readily apparent (Figure 22b).

Semidiurnal barotropic spring-neap forcing is intermittently in-and-out of phase, at both sites, suggesting some remote baroclinic forcing (Figure 23). Phase-lag correlations were determined as for the diurnal band. The scaled semidiurnal depth-mean band-power amplitudes vary greatly from the seasonal spring-neap surface levels. Fortnightly phase-lags are inconsistent, and for 3-month periods range from 0 to 4 days at Slope (inter-annual average of 2.3 days), and from

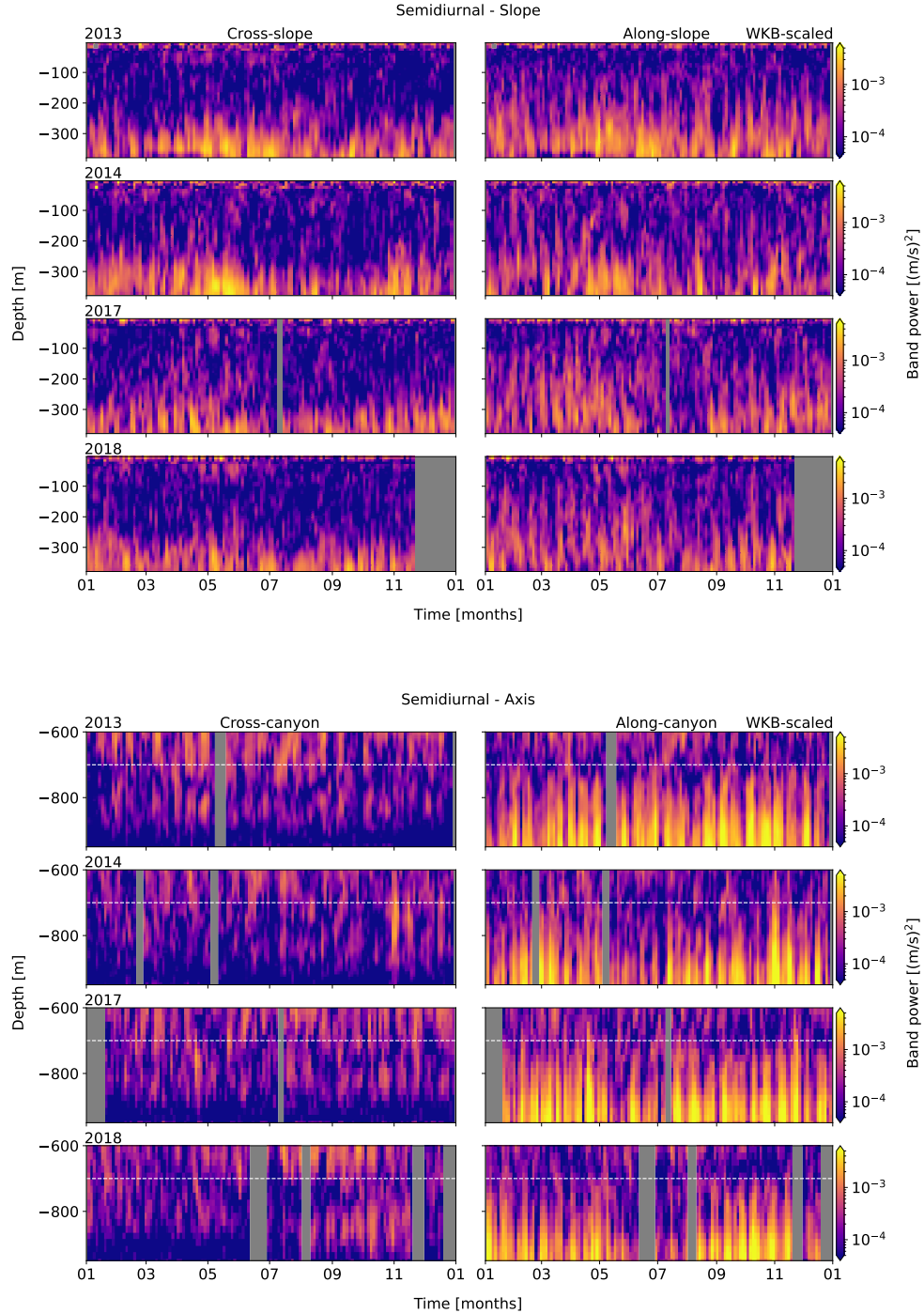


Figure 22. Band-integrated semidiurnal PSD for Slope (upper) and Axis (lower), from WKB-scaled horizontal velocity data. Cross- (left) and along-slope/canyon (right) components are shown. Each row represents an analysis year, labelled at upper-left.

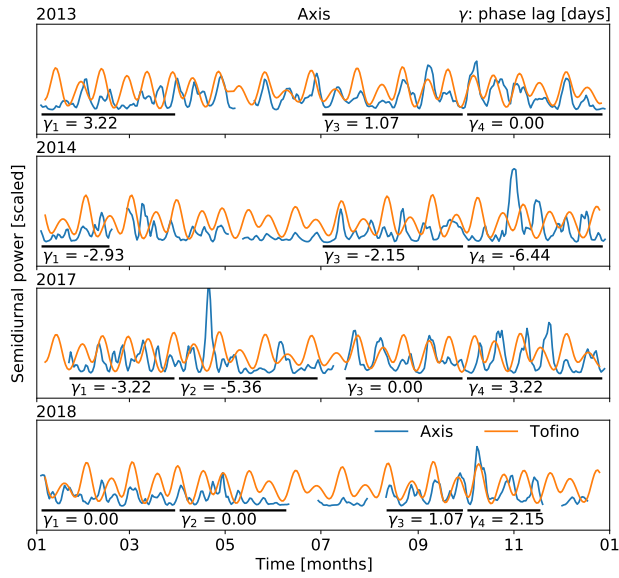
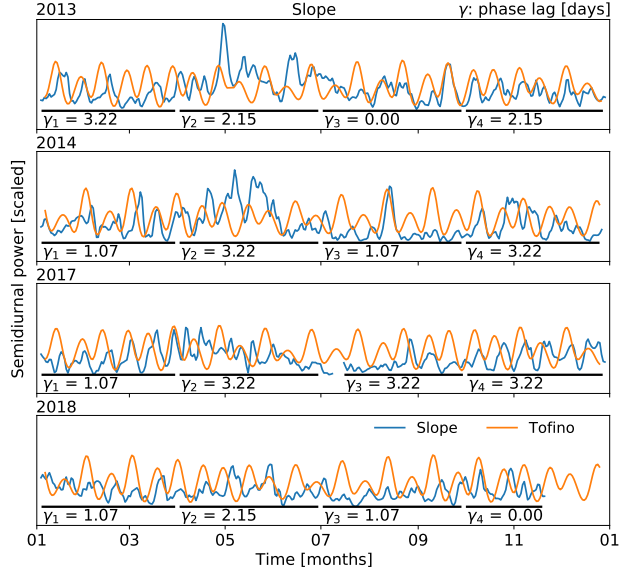


Figure 23. Semidiurnal barotropic forcing comparison. Phase and amplitude (scaled) comparisons for band-integrated power of semidiurnal surface level data (Tofino, orange) and WKB-scaled depth-mean semidiurnal power (blue) at Slope (top) and Axis (bottom). Black bars indicate seasonal correlation ranges. Though the instrument amplitude is highly irregular, there is a variable phase lag that suggests a mix of local barotropic and remote baroclinic forcing.

0 to 6 days at Axis (inter-annual average of 2.8 days). The irregularity of the

phase-offset suggests a mix of local barotropic and remote baroclinic forcing.

5.2.5 Continuum

Seasonality of IW continuum energy ($7.00 \times 10^{-5} - 1.20 \times 10^{-4}$ Hz) at Slope is inter-annually consistent, heightened in spring through early-summer, and again through the fall (Figure 24a). At Axis, seasonality is less apparent, though there is generally more activity in the fall (Figure 24b).

At both sites, the observed continuum amplitude is higher, and the spectral slope more negative, as compared to the open-ocean GM spectrum (Figure 25). For near-bottom depth-specific time series of WKB-scaled PSD (Slope -300 m; Axis -900 m), a power law of af^b was fit to the continuum frequency range and smoothed in two week intervals, resulting in a time series of power law amplitude (a) and slope (b). A similar fit was applied to the open-ocean GM spectrum (its energy halved to compare with u and v components), to find $a_{GM,0.5} \approx 2.7 \times 10^{-9} \text{ m}^2\text{s}^{-2}\text{Hz}^{-1}$ and $b_{GM,0.5} \approx -2.1$. At both sites, observed a ranges within $2 - 5 \times 10^{-9} \text{ m}^2\text{s}^{-2}\text{Hz}^{-1}$, and b within -2.0 – -2.3, similar but generally higher than open-ocean GM values. Time series of power law amplitude and slope are strongly correlated, each a rough copy of depth-mean continuum depth-band power seasonality (not shown).

Elevated near-topography continuum energy leads to enhanced dissipation rates, ε , at both sites (Figure 26). WKB-scaled continuum energy was 'whitened' over the continuum frequency range - its power multiplied by f^2 - then averaged to find mean continuum energy, E_c , in depth and time. Determined similarly, a mean value of open-ocean GM energy was found to be $E_{GM} \approx 8.1 \times 10^{-9} \text{ m}^2\text{s}^{-2}\text{Hz}$. The ratio of E_c/E_{GM} yields non-isotropic E_c amplitudes up to $7 \times E_{GM}$ near topography, while away from topography E_c levels fall to equal or below that of E_{GM} (not shown). From IW interaction theory (Althaus et al., 2003), dissipation estimates were calculated from the WKB-scaled E_c fits as:

$$\varepsilon = \varepsilon_0 \frac{N_0^2}{N_{GM}^2} \frac{\langle E_c^2 \rangle^2}{\langle E_{GM}^2 \rangle^2} f(R_\omega) \quad (19)$$

where $\varepsilon_0 = 4.1 \times 10^{-11} \text{ W/kg}$, $\langle E_c^2 \rangle^2/\langle E_{GM}^2 \rangle^2$ is the measured ratio of continuum energy to GM energy over the same frequency range, and the upper bound

$$f(R_\omega) = \left(\frac{R_\omega + 1}{R_\omega} \right)^2 \left[\cosh^{-1} \left(\frac{N_0}{f} \right) + \frac{25 \cos^{-1}(f/N_0)}{\sqrt{R_\omega}} \right] \quad (20)$$

is an energy ratio as defined by Sun and Kunze (1999), with $R_\omega = 2.13$ (Kunze et al., 2002) for a continuum with predominantly semidiurnal forcing (to be discussed). Results exceed 10^{-8} W/kg near topography, fluctuating with continuum energy seasonality. Away from topography, dissipation is on the order

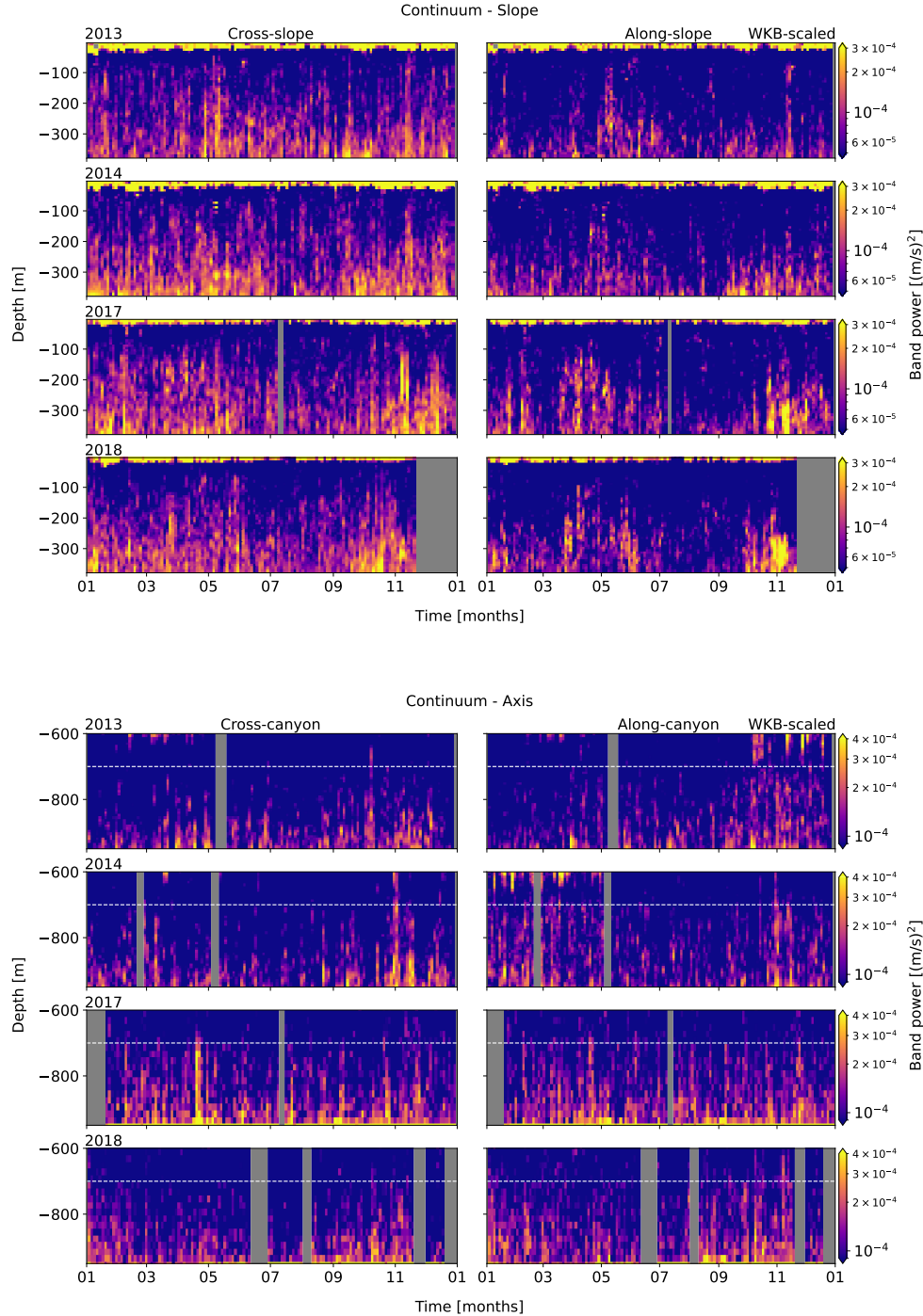


Figure 24. Band-integrated continuum PSD for Slope (upper) and Axis (lower), from WKB-scaled horizontal velocity data. Cross- (left) and along-slope/canyon (right) components are shown. Each row represents an analysis year, labelled at upper-left.

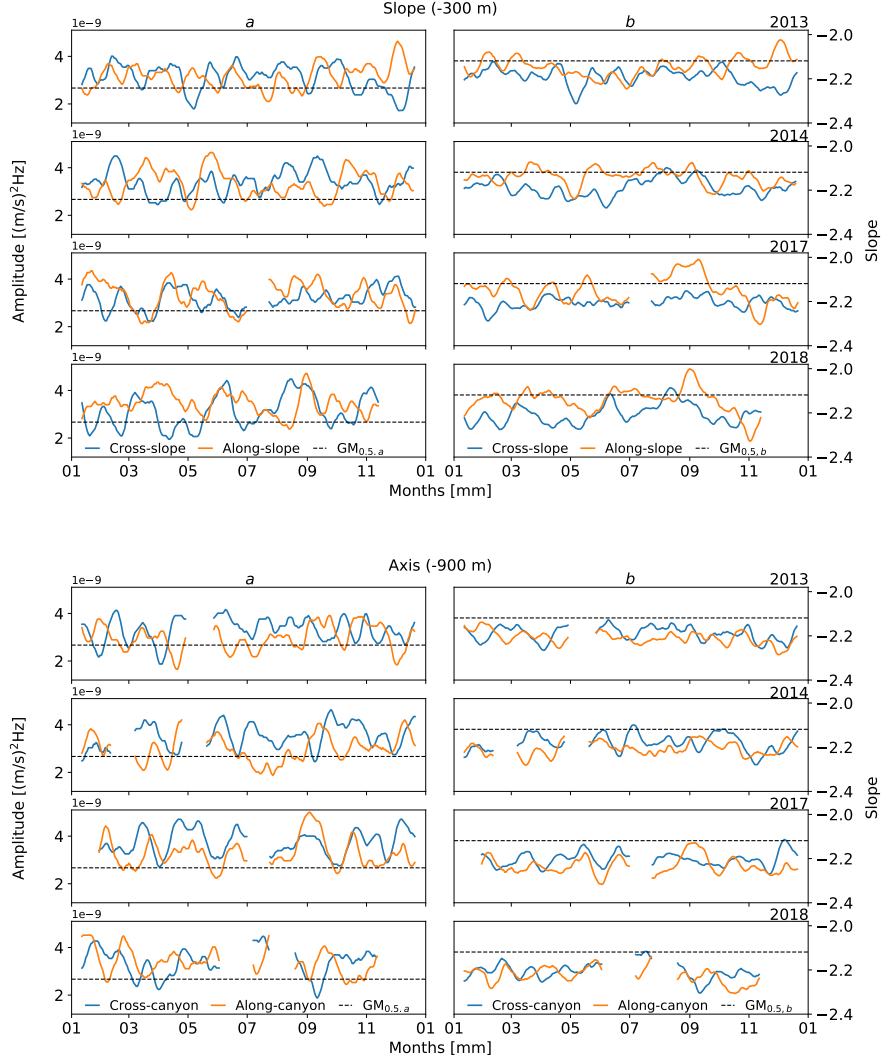


Figure 25. Time-series of continuum power law fits. Continuum amplitude, a (left), and slope, b (right), of power law ($a f^b$) fits to lower-depth WKB-scaled PSD, at Slope (top) and Axis (bottom). For each site, each row is a year, labelled upper-right. Time series were smoothed over two weeks. Compared to GM, amplitudes are elevated up to $2 \times$ GM in the centre of the enhancement layer, with slopes down to -2.3.

of 10^{-9} W/kg or less. Turbulent eddy diffusivities, κ , are similarly elevated near topography (Figure 26). From ϵ , diffusivity was calculated as by Kunze et al. (2002), as:

$$\kappa = \frac{\gamma \varepsilon}{N_0^2} \quad (21)$$

where $\gamma = 0.2$ is the mixing efficiency for high-Reynolds-number turbulence.

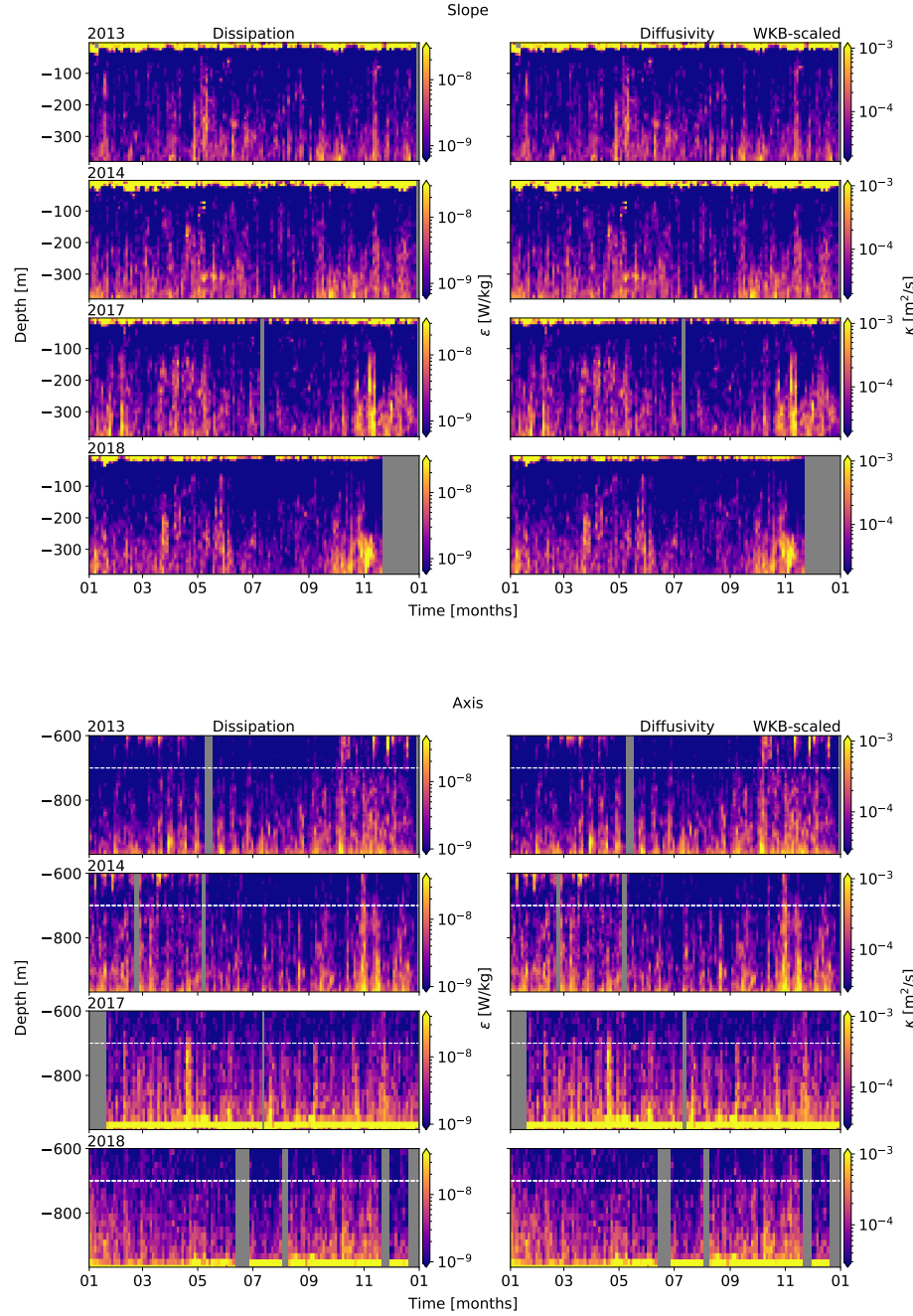


Figure 26. Dissipation rates (left) and turbulent eddy diffusivity (right), for WKB-scaled horizontal velocity spectra at Slope (top) and Axis (bottom). Both dissipation and diffusivity are heightened near topography.

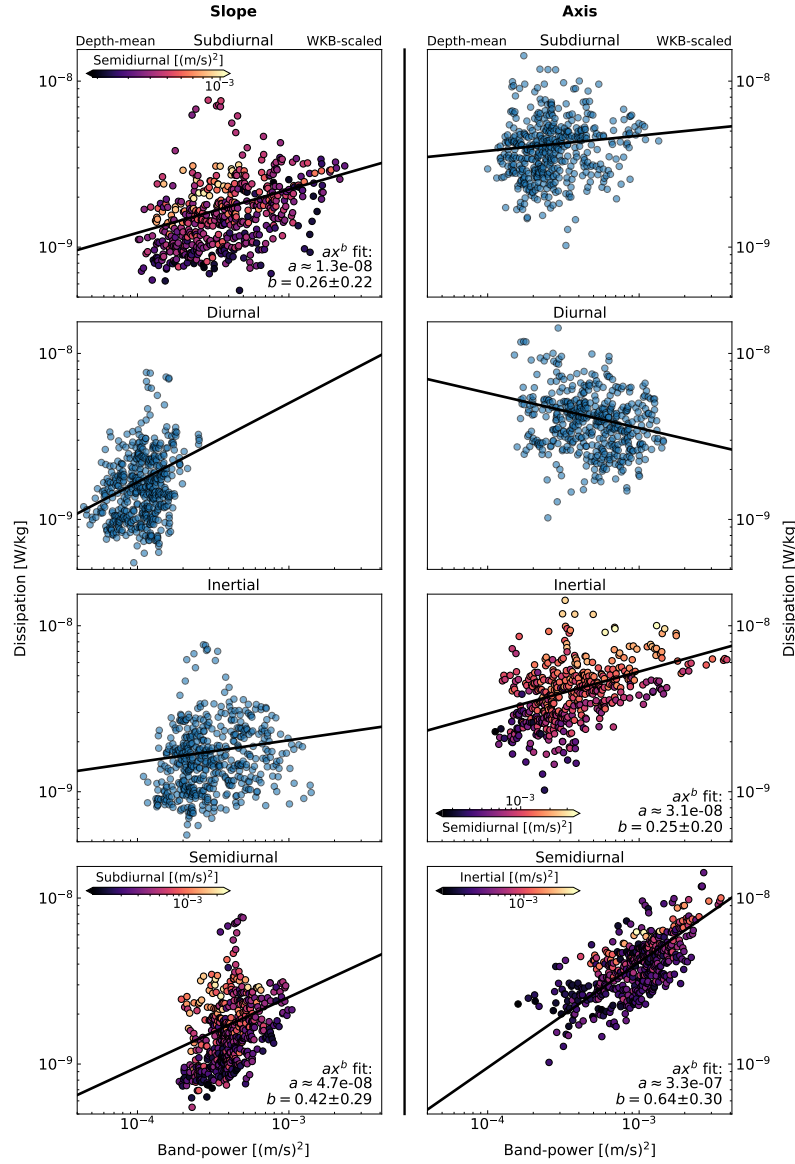


Figure 27. Dissipation power law fits. Scatter plots are for depth-mean WKB-scaled depth-band power at Slope (left) and Axis (right), all years. Frequency constituents are listed for each row, as sub-diurnal (top), diurnal (second), NI (third), and semidiurnal (bottom). Black lines indicate the power law fit, listed in the lower-right of each frame. For each site, the two most likely contributors are coloured by the strength of the other.

Turbulent eddy diffusivities reach $10^{-3} \text{ m}^2\text{s}^{-1}$ near topography, again fluctuating with continuum energy seasonality. Away from topography, diffusivity values are on the order of $10^{-5} \text{ m}^2\text{s}^{-1}$ or less, consistent with open-ocean values (Gregg, 1989; Kunze et al., 2002).

Dissipation seasonality (derived from continuum energy seasonality) is correlated with semidiurnal forcing at both sites, with secondary contributions from the sub-diurnal band at Slope, and the NI band at Axis (Figure 27). Dissipation seasonality correlations were determined as for NI wind forcing, for each constituent (not shown). At Slope, the semidiurnal band shows moderate correlations throughout the year, and strong correlations in the spring, while the sub-diurnal band shows weak to moderate correlations in both winter and spring. At Axis, the semidiurnal band is strongly correlated all year, while the NI band is moderate to strongly correlated in the spring and fall. There is no apparent fortnightly modulation of continuum energy or vertical scale associated with diurnal or semidiurnal spring-neap effects. To further quantify these relationships, power laws of ax^b were fit to scatter plots of depth-mean dissipation-power time series for each frequency constituent. The process was bootstrapped for improved uncertainties. At both sites the semidiurnal band shows the best fit, and is stronger at Axis. The sub-diurnal band at Slope, and the NI band at Axis, are secondary contributors with less obvious fits. Both the semidiurnal and secondary bands contribute to higher dissipation as they increase, but they do not drive each other. The power law fits for semidiurnal driven dissipation are $\epsilon \sim M_2^{0.42 \pm 0.29}$ at Slope, and $\epsilon \sim M_2^{0.64 \pm 0.30}$ at Axis.

Multi-variate analysis improves power law fits, reinforcing the importance of the secondary contributing constituents (Figure 28). Secondary constituents were added to the semidiurnal power law fits as $ax_1^b + cx_2^d$, where x_1 is the depth-mean semidiurnal band-power and x_2 is the secondary contributing band. The process was bootstrapped for improved uncertainties. Multi-variate power laws relationships of $\epsilon \sim M_2^{0.83 \pm 0.17} + \text{Sub}_{K1}^{0.59 \pm 0.13}$ and $\epsilon \sim M_2^{1.47 \pm 0.48} + \text{NI}^{0.24 \pm 0.06}$ were found for Slope and Axis, respectively. At Slope, the purely semidiurnal fits are generally overestimated, and conservative in periods of high and low dissipation, while multi-variate fits are less conservative and better reflect seasonal variability. At Axis, purely semidiurnal fits are reasonable, but generally underestimate dissipation in 2017 and 2018, while multi-variate fits are fairly accurate in all years. A percent-good metric indicates the multi-variate fit is closer to ϵ for 68% of data points at Slope, and 62% at Axis.

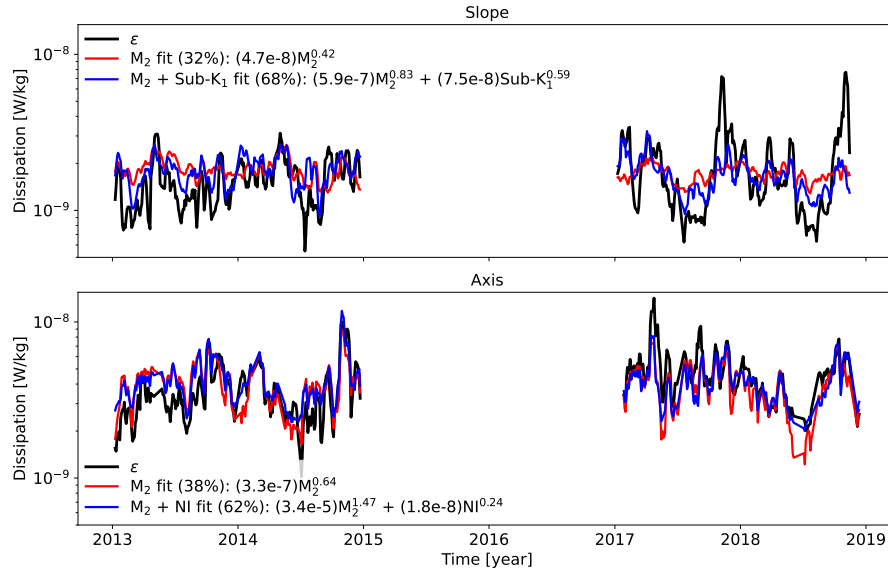


Figure 28. Dissipation multi-variate power law fits for Slope (top) and Axis (bottom). Comparison time series of depth-mean WKB-scaled dissipation (black), semidiurnal power law fits (red), and multi-variate power law fits (blue). Percent good is listed for each fit, as a measure of which fit line is closest to ϵ at each time step. Dissipation (black) time-series shows the seasonal trend towards a summer lull, with more energetic fall events in later years. The purely semidiurnal fits (red) are conservative in estimating periods of high and low energy, at Slope, and often underestimate at Axis. The multi-variate fits (blue) are improved, less conservative in estimating extremes at Slope, and fairly accurate at Axis.

5.2.6 Shoulder

The near- N spectral shoulder (here defined between $2.00 \times 10^{-4} - 1.00 \times 10^{-3}$ Hz) is typically unresolved in oceanographic power spectra, and the 15-minute data used in this study only partly expose this feature. To properly analyse the shoulder, 2-second data from the 75 kHz RDI instruments were obtained to allow for increased Nyquist frequency. The data for this high-frequency range were then processed similarly to the other frequency constituents. Shoulder depth-band power is elevated near topography, though less uniformly than for lower-frequency constituents (Figure 29). At Slope, shoulder power is mostly cross-slope and rectilinear, and somewhat intermittent in its depth-dependent enhancement. At Axis, shoulder power is isotropic, and its depth-dependent enhancement more vertically uniform than at Slope. Shoulder power seasonality at Slope is subtle, somewhat heightened in the spring and fall, with intermittent brief pulses that are inconsistent in both depth and time. At Axis, there is subtly increased energy in the fall.

However, there are multiple issues with interpreting shoulder power seasonality at Axis. During 2013 and 2014, there were adjustments to ADCP beam

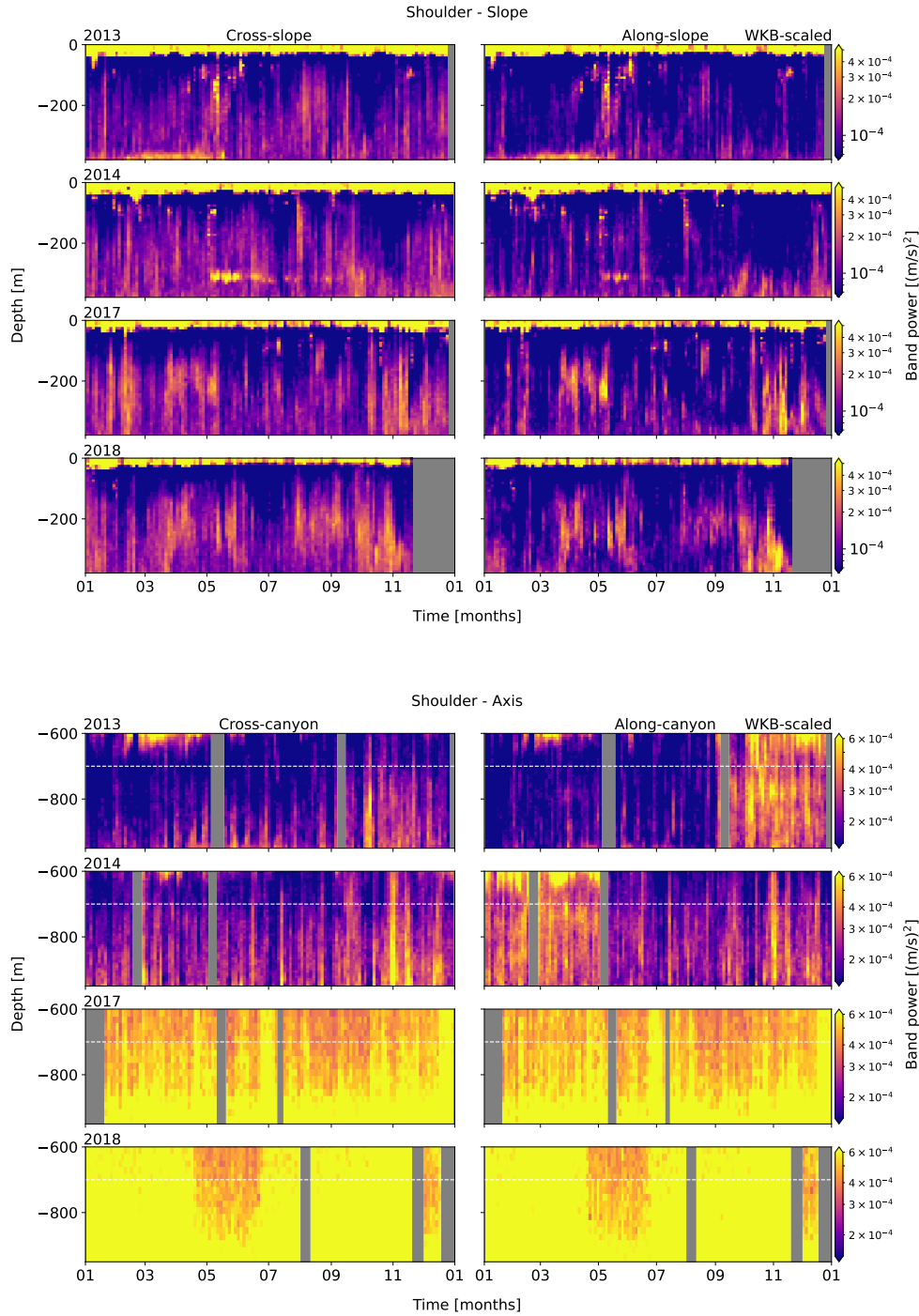


Figure 29. Band-integrated shoulder PSD for Slope (upper) and Axis (lower), from WKB-scaled horizontal velocity data. Cross- (left) and along-slope/canyon (right) components are shown. Each row represents an analysis year, labelled at upper-left.

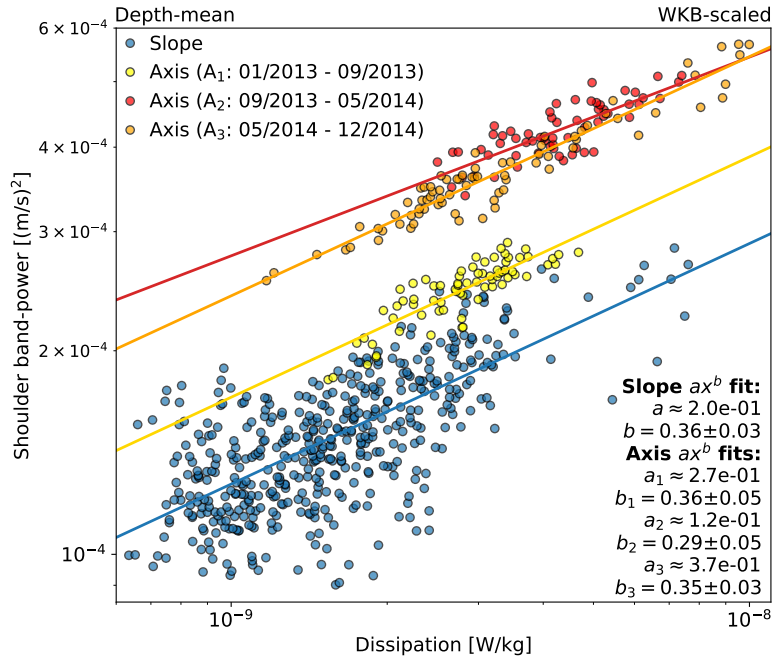


Figure 30. Power law relationship between dissipation and the spectral shoulder. Inter-annual depth-mean scatter plot for WKB-scaled dissipation and shoulder depth-band power, for Slope (blue) and Axis (yellow, red, orange). Slope data is for all four analysis years. Axis data is separated into three variance periods determined by instrument swaps and adjustments, for 2013 and 2014. All power law slopes agree within uncertainty, suggesting strong correlation to dissipation that does not depend on site topography.

orientation (2013/05 and 2014/05) relative to canyon topography, an instrument swap (2014/05), and a switch from 4- to 3-beam solutions (2013/05), somehow resulting in distinct periods of higher variance (though this did not affect lower frequencies, likely due to their broader horizontal scale). These periods are defined as: A₁ (2013/01 - 2013/09), while the first RDI 75 kHz instrument was operating with a 4-beam solution; A₂ (2013/09 - 2014/05), after the same instrument was adjusted to a 3-beam solution, showing heightened variance up to 3× A₁; and A₃ (2014/05 - 2014/12), after a new 75 kHz 3-beam instrument was swapped in, and variance was lowered to up to 2× A₁. It is possible that the difference between A₂ and A₃ could be physical, as there is a coinciding drop in continuum energy; possible only if continuum energy is not (or at least not as much) affected by the instrument adjustments, which seems to be indicated in the comparative variance of raw spectra. When an orientation adjustment coincided with a variance jump (as in 2014/05), the rotation was minimal (up to ∼20°), suggesting the wave field would have to be

quite asymmetric to result in such a difference; this is unlikely. In 2017 and 2018, use of Nortek 55 kHz instruments at Axis does not allow for clear resolution of the spectral shoulder, as those instruments' noise floors are higher than that of the previous 75 kHz ADCPs (Figure 12). Re-evaluation of the spectral shoulder variance at Axis is worthwhile, but beyond the scope of this study.

There is a distinct power law relationship between dissipation and the spectral shoulder (Figure 30). Power law fits for WKB-scaled depth-mean dissipation and shoulder depth-band power (P_{Sh}) were determined as for the continuum analysis of Section 5.2.5. At Slope, there is a reasonable fit of $P_{Sh} \sim \epsilon^{0.36} \pm 0.03$ for all four years. At Axis, a power law was fit to each of the three variance periods in 2013 and 2014. Though amplitudes vary between periods, power law slopes are similar, with $P_{Sh} \sim \epsilon^{0.36 \pm 0.05}$, $P_{Sh} \sim \epsilon^{0.29 \pm 0.05}$, and $P_{Sh} \sim \epsilon^{0.35 \pm 0.03}$ for periods A₁, A₂, and A₃, respectively. Power law slopes at both Slope and Axis all agree within uncertainty (averaging $P_{Sh} \sim \epsilon^{0.34 \pm 0.08}$), suggesting a strong connection between spectral shoulder energy and turbulence that does not depend on site topography.

6 Discussion

6.1 Canyon axis mean currents

The periodic (~ week) up-canyon shoaling mean flow at Axis (between -700 and -900 m), with its underlying near-bottom down-canyon layer, is notable for its seasonal and inter-annual consistency and circulation implications (close to zero net mean flow), important for understanding sediment transport and physical-biological coupling influencing VICS productivity (Xu & Noble, 2009). In previous biological studies at Barkley Canyon (Cabrera et. al, 2018; Chauvet et al., 2018), a two-layer flow system was noted similar to that of Hudson Canyon (Hotchkiss & Wunsch, 1982) and Monterey Canyon (Xu & Noble, 2009); the systems were attributed to circulation cells caused by along-canyon pressure gradients driven by consistent large-scale quasi-geostrophic along-shelf regional currents, similar to those observed at Slope. The shoaling of these currents was observed with periodicity ranging from semidiurnal (Monterey Canyon) to $>$ than a few days (Hudson Canyon), and found to shoal at an angle similar to that of the up-slope gradient (Hotchkiss & Wunsch, 1982; Petrunio et al., 1998; Xu & Noble, 2009). Tidal rectification, where tides force an up-slope pressure gradient (Garrett, 2004), could also drive a periodic mean up-canyon flow. The associated near-bottom (< 50 m) down-canyon flow could also be linked to turbidity currents and river-flood-induced underflows, that

occur as shelf sediment descends through canyons to the ocean interior (Xu & Noble, 2009; Chauvet et al., 2018). At Barkley Canyon, where large-scale regional mean currents move consistently along-slope across the mouth and rim of the canyon, this seems a likely explanation; however, tidal rectification and turbidity currents cannot be ruled out.

To associate the observed mean flow characteristics with these potential forcing mechanisms, correlations were computed for the observed along-canyon periodicity and mean currents at Slope, fortnightly spring-neap tidal influence, and depth-mean semidiurnal depth-band power. Correlations are inconsistent (not shown), and do not suggest forcing by these sources. However, though there is no obvious connection to diurnal or semidiurnal spring-neap forcing, estimates of total lower-canyon transport (below -700 m) from depth- and time-mean annual velocities result in near-zero net up-canyon flow (annually between 0.004 - 0.005 m/s), potentially consistent with tidal rectification theory.

Though along-canyon mean flow systems have been noted at other canyons, the periodicity and attributed forcing comparisons at Barkley Canyon do not align with other studies. It seems most likely that this circulation is driven by the strong regional mean currents that exist at Slope, though tidal rectification and turbidity currents may contribute. It is possible that such circulation may be common in shelf-incising canyons, but that forcing is dependent on unique site characteristics and regional physical processes, and so is difficult to determine. Further evaluation is necessary, and beyond the scope of this study.

6.2 Tidal forcing

The diurnal and semidiurnal tidal constituents are two of the greatest sources of IW energy, and affect mean currents, mixing, IT and baroclinic shelf wave propagation, and VICS circulation and productivity (Crawford & Thomson, 1984; Cummins & Oey, 1997).

For the diurnal constituent, there is elevated energy in the late-spring and summer. Results are consistent with previous studies in the region; Drakopolous and Marsden (1993) associated strengthened diurnal tidal flow over the VICS with increased stratification in summer, while Cummins et al. (2000) suggest diurnal currents are seasonally responsive to the large-scale spring shift to equatorward, upwelling-favourable, mean currents. Xu and Noble (2009) found inter-annually consistent K_1 currents in Monterey Canyon that peaked relative to the annual cycle of spring-neap tidal forcing, as observed.

As the diurnal (and sub-diurnal) frequency is sub-inertial, diurnal IT are

evanescent (trapped) to topography north of their turning latitude ($\sim 30^\circ\text{N}$), unable to radiate offshore. This is consistent with the likely barotropic forcing observed; Cummins and Oey (1997) found that trapped diurnal IT generation was prevalent on the VICS adjacent continental slope, similar to other Pacific slopes (Rudnick et al., 2015) and seamounts (Robertson et al., 2017). It is unlikely for there to be incident baroclinic diurnal IW or IT unless they propagate along the shelf. However, if a diurnal spring-neap phase-lag of up to a day is present, as potentially observed at Slope, this suggests a baroclinic generation site within about 200 km, based on a K_1 mode-1 wave speed of about $c_1 \sim 2.0 \text{ m/s}$ (Crawford & Thomson, 1984). One candidate would be diurnal shelf waves generated by oscillatory tidal currents near the mouth of the Juan de Fuca Strait ($\sim 100 \text{ km}$ east) that propagate poleward along the VICS (Crawford & Thomson, 1984; Flather, 1988). Confirmation of such waves would require additional instruments along the shelf, and is beyond the scope of this study. Other regions thought to be productive for baroclinic diurnal waves are either disconnected from the shelf (e.g. the abyssal Juan de Fuca Ridge) and cannot propagate sub-inertially to Barkley Canyon (Lavelle & Cannon, 2001), or too distant for the observed phase-lag (e.g. Mendocino Escarpment, 900 km south; Morozov, 2018). As there is enough uncertainty in the correlations that the phase-lag could effectively be null, and considering the vertically linear structure present, it is likely that the diurnal band is primarily forced by the local barotropic spring-neap cycle, with possible seasonal contributions from shelf-waves, mean current interactions, or stratification.

In contrast, the semidiurnal constituent is locally super-inertial, able to freely propagate away from topography as IT. There could be incident remote semidiurnal IT at Barkley Canyon, contributing to the highly variable response. For a semidiurnal phase-lag up to four days, as potentially observed at Slope, a regional mode-1 M_2 phase speed of $c_1 \sim 3.0 \text{ m/s}$ (Zhao et al., 2016) suggests a baroclinic generation site up to 1000 km away. A likely candidate is the Mendocino Escarpment running E-W off of Northern California, one of the strongest generation sites for low-mode semidiurnal IT in the northeast Pacific (Althaus et al., 2003; Arbic et al., 2012; Zhao et al., 2017; Morozov, 2018). Strong tide-topography generated northward propagating mode-1 M_2 IT, along with the escarpment's location about 800 km due south of Barkley Canyon (~ 3.5 days), agree reasonably with the observed phase lag. Other potential semidiurnal IT generation sites are closer (e.g. the mouth of Juan de Fuca Strait $\sim 100 \text{ km}$, or the abyssal Juan de Fuca Ridge $\sim 400 \text{ km}$), or are somewhat obstructed by land (e.g. the Haida Gwaii Islands to the north), but could contribute.

Furthermore, for free IW and IT, such as incident semidiurnal IT, the criticality of the impacted topography can lead to focusing and breaking, or reflection. Barkley Canyon is generally supercritical or near-critical to incident semidiurnal IT (Figure 4). Critical slope regions were determined from the gradient of bathymetry data obtained from the National Oceanic and Atmospheric Administration (NOAA) National Centre for Environmental Information, as 3 arc-second resolution mean sea level depth. At the Slope mooring, the local slope is $\beta \approx 0.060$, supercritical to the semidiurnal propagation angle $\alpha_{M2} \approx 0.026$ at that depth (Figure 5). This suggests downward reflection (CW) and focusing of incident semidiurnal IT. The Slope mooring sits adjacent to a large near-critical region below the shelf-break (Figure 4), which, along with the VICS itself, is another source of observed downward semidiurnal energy (Drakopoulos & Marsden, 1993). At other slope sites, there is evidence of elevated near-bottom energy-flux associated with both semidiurnal IT generation and incident reflection, with similar vertical scales within a few hundred metres AB (Terker et al., 2014; Xie & Chen, 2021). For the Axis mooring on the canyon floor, local criticality is $\beta \approx 0.019 < \alpha_{M2} \approx 0.036$ (Figure 5). As such, this portion of the canyon floor is subcritical to semidiurnal IT, suggesting upward reflection (CCW). However, as the canyon walls are generally supercritical, and the surrounding floor is near-critical (Figure 4), the propagation of semidiurnal IT at Axis is likely complex. Xu and Noble (2009) found that deep in Monterey Canyon semidiurnal IT were not only scattered up-canyon along the subcritical floor, but also reflected down by the supercritical walls, highly focusing semidiurnal energy near the bottom. The potential for scattering, reflection, focusing, and generation of semidiurnal IT all near the Axis mooring could lead to the highly 'channeled' deep-canyon semidiurnal response.

Together, the irregular nature of the semidiurnal spring-neap phase-lag and the potential for critical IT-topography interactions suggests that forcing is a mix of local barotropic and incident IT. As the barotropic tide passes over Barkley Canyon, near-critical slope topography generates and focuses semidiurnal IT, which radiate downward from the shelf-break to the slope and canyon, where further downward reflection and focusing occurs. Remote incident IT are also subject to these effects, and alter observed spring-neap phase based on their origin, likely Mendocino Escarpment to the south. Finally, as the little annual seasonality in the local barotropic spring-neap forcing cannot explain large-scale inter-annual features in the observations, such as the subtle yet consistent spring increase in semidiurnal energy at Slope, secondary contributors may include seasonal changes to stratification (Drakopoulos & Marsden, 1993) and mean currents (Cummins et al., 2000).

6.3 Near-inertial forcing

NI IW generated by wind events are thought to be significant contributors to mixing in the deep ocean, of similar magnitude to the conversion of barotropic tide to baroclinic internal tide energy (Alford et al., 2012). As such effective contributors to deep ocean energy, it is interesting that NI band-power can be so strongly attenuated with depth at Slope, while still eliciting a deep response at Axis. The timing of these events is linked, so the difference in topography likely modulates the response. Thomson et al. (1990) found that NI IW become increasingly attenuated as they approach slopes, absorbed by strong vertical shear in the background flow associated with topographically trapped oscillations. Yet observed NI IW energy is enhanced near the canyon floor, not attenuated. Alford et al. (2016) note that canyon walls confine the typically circular motion of NI waves, forcing them rectilinearly along-canyon.

It may be that canyon topography uniquely effects the modal structure of ML generated NI waves. Mode-1 amplitudes up to 0.6 m/s occur after notable wind events, similar to findings by Jarosz et al. (2007) in DeSoto Canyon, who found that while low modes generally dominate, more NI activity is observed when the ML is thin and high modes are prevalent. Alford et al. (2016) note that high mode waves propagate downward and equatorward, while low mode waves contribute more to lateral propagation of NI energy. Ultimately, the downward propagation of NI IW is difficult to characterise, as there are so many factors to consider, including topography, seasonal thermocline thickness, β -plane effects, and near-surface mesoscale vorticity adjusting local f_0 (Alford et al., 2016). Potential secondary forcing could be mean currents or lee waves of NI frequency across the mouth or rim of the canyon, where topographic attenuation of downward NI energy may be reduced due to the relative openness of those areas, driving deep along-canyon NI currents.

Regarding the delayed NI deep response to wind events, D'Asaro (1995) made a similar observation of an 8-10 day event, and theorised that divergence-forced NI pumping at the ML base causes oscillating pressure gradients in the thermocline, accelerating NI currents at depth. The rate of vertical energy transfer depends on the horizontal scale of the ML NI currents, with smaller horizontal scale ML currents propagating vertical energy faster. As vertical modes have progressively slower horizontal group velocities, the low modes propagate their energy away, first. As the low mode energy propagates away, the available energy and horizontal scale of the ML inertial currents decreases. Vertical energy propagation into the thermocline increases accordingly, with a notable maximum associated with a timescale of the departure of modes 1 and 2 (up to 10-20 days), described as 'inertial beating', after which the deep

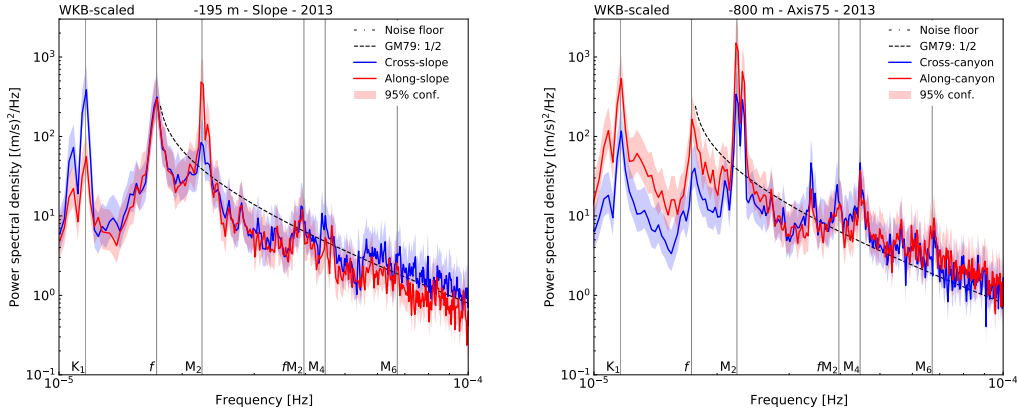


Figure 31. High frequency-resolution mid-depth PSD of WKB-scaled horizontal velocity data, for Slope (left) and Axis (right), in 2013. Frequency scale is zoomed to the tidal range. There are no additional peaks or apparent blue-shift for the NI constituent, suggesting local forcing.

response rapidly increases and NI energy is evenly distributed between the upper thermocline and lower depths (Gill, 1984; D’Asaro, 1995; Zervakis & Levine, 1995). The beta effect can also decrease the north-south horizontal wavenumber, l , over time, further decreasing the horizontal scale of the ML NI currents and increasing downward NI energy transfer. The radiation of NI energy to deep water is also occasionally associated with ‘inertial jets’ of CW relative vorticity originating near the upper pycnocline, possibly induced by mesoscale fronts (Kunze, 1985; D’Asaro, 1995; Zhai et al., 2005; Alford et al., 2016).

The results suggest that NI forcing is complex, dependent on variable characteristics of both wind events and ML processes, leading to highly intermittent seasonality, below. Small (~ 100 km) southward cold fronts and lows with considerable CW NI rotation are the most significant sources of ML NI flux, even more-so than synoptic-scale systems, and occur most often, yet intermittently, in fall and early-winter (D’Asaro, 1985; Alford, 2001; Voelker et al., 2020). Remote forcing is also possible, as free NI IW generated at the base of the surface mixed-layer must propagate equatorward due to the effects of turning latitudes (Alford et al., 2016). There is often a blue-shift of the f spectral peak associated with remote NI forcing (Garratt, 1977; Voelker et al., 2020); however, high frequency-resolution spectra (Figure 31) do not resolve any additional NI peaks. Wind forcing correlations may be further complicated by the location of the wind data buoy, 50 km north of Barkley Canyon. Regardless, strong qualitative and moderate quantitative correlations suggest that

the NI observations are most responsive to wind events when the ML is thin and high-mode contributions are prevalent, particularly in the late-summer and fall. Jarosz et al. (2007) noted that seasonally variable pycnocline and ML depths can modulate NI energy by up $12\times$ when the ML is thin, affecting the stratification-dependent modes strummed by the wind induced ML NI currents. All in all, accurate quantification of NI energy is difficult. To summarise the efficacy of attempting to characterise vertical NI processes, Alford et al. (2016), when discussing the foundational Ocean Storms Experiment (D'Asaro, 1995), stated that “neither the decay of mixed-layer motions nor the rate of energy transfer into the deep ocean can adequately be predicted for the best-documented storm response on record”; needless to say, additional research is necessary.

6.4 Continuum-dissipation estimates

Topographic focusing of low-frequency IW and IT enhances energy, elevating the continuum amplitude and driving mixing (Polzin, 2004). This is indicated by the heightened amplitudes and steep spectral slopes of the observed continuum, as compared to open-ocean GM values (Figure 25). As IW energy cascades from low- (tidal and sub-inertial) to high-frequency processes, continuum energy seasonality should reflect this transfer (Polzin, 2004). At both sites, continuum energy seasonality correlations and power law fits indicate the semidiurnal constituent is the greatest contributor to dissipation; secondary contributors are the sub-diurnal band at Slope, and NI band at Axis. There are likely lesser contributions from other constituents. For continental slopes, mean currents and semidiurnal IT have both been noted to contribute to increased near-bottom dissipation rates (Nash et al., 2007; Kunze et al., 2012), as observed. Similarly, in submarine canyons, the semidiurnal constituent has been found to be the primary contributor to seasonal, near-bottom mixing (Kunze et al., 2002; Waterhouse et al., 2017); however, there is a lack of evidence for the observed deep-canyon NI IW energy, as discussed in Section 6.3. Also evident is the non-isotropic nature of the continuum, in contrast to a theoretical GM open-ocean IW field, though this departure from theory is not surprising considering the strong topographic guiding of flow.

As it is difficult to quantify turbulence, it is hoped that a connection to semidiurnal (and secondary constituent) energy may be useful for models that may not have access to data that can resolve such high-frequency processes, in slope and canyon regions. The multi-variate power law fits were found to be $\epsilon \sim M_2^{0.83 \pm 0.17} + \text{Sub}_{K1}^{0.59 \pm 0.13}$ and $\epsilon \sim M_2^{1.47 \pm 0.48} + \text{NI}^{0.24 \pm 0.06}$, for Slope and Axis, respectively. This builds on similar results by Klymak et al. (2006) at the Hawaiian Ridge, who found that near the ridge dissipation scaled with

semidiurnal energy as $\epsilon \sim M_2^{1.0 \pm 0.5}$. However, it is not enough to link dissipation to IW and IT driven continuum energy, alone, as there are many spatially and temporally variable regional processes that may also contribute, such as large-scale ocean circulation, biogeochemical cycles, weather, and long-term climate (Kunze, 2017). Furthermore, turbulence may be forced intermittently by these phenomena (Klymak et al., 2006), making it difficult to attribute individual contributors over long periods. Use of the observed fits for modelling should be considered with these issues in mind, and improvements could be the subject of further research.

6.5 Spectral shoulder energy

The near- N spectral shoulder is a well known, yet often unresolved feature in ADCP velocity spectra. As early as 1975, Pinkel described a prominent near- N peak that widened with depth, ascribed to IW-buoyancy ringing, yet beyond the next decade (Kase & Clarke, 1978; Levine et al., 1983) subsequent observations are brief, and temporally sparse (D'Asaro et al., 2007; Pinkel, 2014; Alford et al., 2016). The long-term, high-frequency sampling in this study allows for a high Nyquist frequency and low noise floor that fully expose the shoulder, continuing the discussion. Observations indicate that shoulder energy is intermittently depth dependent at Slope, and more uniformly so at Axis, similar to Pinkel's (1975) findings. There is subtle shoulder energy seasonality at both sites, being generally stronger in the fall, with correlations and power law fits suggesting that shoulder energy is tied to the continuum, and therefore dissipation. This agrees with previous theories, arguing that the near- N shoulder is a result of an enhanced cascade of energy from low- to high-frequency turbulent processes due to resonant wave-wave interaction, where energy collects at and above the “resonant buoyancy frequency” - approximately the depth-mean value of N below the buoyancy variable thermocline (Leder, 2002). In this study, $N_0 = 4.03 \times 10^{-4}$ Hz (averaged around -900 m and varying insubstantially when expanded to the lower thermocline), central to the observed shoulder, and similar to the ~ 2 cph value of N_0 that defined the spectral shoulder (2 - 5 cph) of Kase and Clarke (1978), who modelled the near- N response with data from the GATE experiment.

However, seasonal forcing of the near- N spectral shoulder is inconsistent between studies. At Barkley Canyon, correlations and power law fits suggest that continuum energy is strongly linked to spectral shoulder energy. As these power law fits overlap within uncertainty for both sites (averaging $P_{Sh} \sim \epsilon^{0.34 \pm 0.08}$), it is possible that this relationship is independent of site topography, possibly due to the relatively small spatial scale of near- N motions. Furthermore, as continuum energy is strongly suspected to cascade from the

semidiurnal constituent (and partially from secondary contributors), the same forcing should apply to the spectral shoulder as the cascade continues. Leder (2002) suggested that solitons forming in the troughs of semidiurnal IT could contribute to near- N energy, but that it is unlikely, and evidence against this theory was provided by D'Asaro et al. (2007) who found no association between shoulder energy and observed solibores. Furthermore, there are no obvious solibores noted in the Barkley Canyon observations. Pinkel (2014) suggested that sub-mesoscale currents could contribute to near- N energy, and both Leder (2002) and Alford et al. (2016) attributed enhanced high-frequency shear to wind-forced NI IW. Forcing by these constituents agrees roughly with the possible secondary contributors to observed continuum energy (sub-diurnal at Slope, and NI at Axis), but is suspiciously lacking semidiurnal influence. It is possible that the near- N spectral shoulder does receive energy from the continuum, but that turbulent processes are so variable, regionally, that forcing is unique to each study site. Properly quantifying the nature of this enhanced cascade of energy is important for better understanding the effects of turbulence and mixing, but is beyond the scope of this study.

7 Summary and conclusions

It was found that there is significant influence from topography on the local IW field at both sites. Continental slope and canyon topography guides flow, with inter-annually consistent, periodic (about a week) up-canyon mean currents (-700 to -900 m) above a near-bottom down-canyon layer. There is frequency-dependent focusing of IW energy, generally up to a factor of 10, 130 m AB at Slope, and up to a factor of 100, 230 m AB at Axis. The near-topography enhancement layer has unique seasonality for individual frequency constituents, and varies little inter-annually. Sub-diurnal and diurnal flows are sub-inertially trapped along topography, and the diurnal band appears to be forced locally (barotropically). The NI band is attenuated near the slope, yet elevated near the canyon bottom, with intermittent forcing that appears linked to regional wind events, high-mode propagation, and the seasonal ML depth. Free semidiurnal IT are focused and reflected near critical topography, and appear to experience both local and remote (baroclinic) forcing. The IW continuum is elevated compared to the open-ocean GM spectrum (up to $7 \times$ GM), with enhanced dissipation (exceeding 10^{-8} W/kg) and diffusivity (exceeding 10^{-4} m²/s) near topography. Dissipation–band-power seasonality correlations suggest a cascade of energy from the semidiurnal constituent, yielding inter-annual power law fits of $\epsilon \sim M_2^{0.42 \pm 0.29}$ at Slope, and $\epsilon \sim M_2^{0.64 \pm 0.30}$ at Axis. Improved fits accounting for secondary constituents (Sub_{K1} at Slope, and NI

at Axis) yield power law relationships of $\epsilon \sim M_2^{0.83 \pm 0.17} + \text{Sub}_{K1}^{0.59 \pm 0.13}$ at Slope, and $\epsilon \sim M_2^{1.47 \pm 0.48} + \text{NI}^{0.24 \pm 0.06}$ at Axis. There is evidence of a near- N spectral shoulder which may obtain energy from the continuum, possibly an additional step in the cascade of energy from low- to high-frequency dissipative processes. The shoulder-dissipation energy seasonality correlations yield an average, site-independent power law fit of $P_{Sh} \sim \epsilon^{0.34 \pm 0.08}$.

Unfortunately, the WKB-stretch scaling applied throughout much of the analysis is based on deep CTD casts that were made nearby (20 km S), but away from topography; the stratification profile captures the surface ML and pycnocline, but does not account for stratification adjustment near the slope or in the canyon (Figure 8). Hotchkiss and Wunsch (1982) noted increased stratification near areas of high 'topographic relief', such as the shelf-break and slopes. These highly stratified turbulent layers may more strongly experience the effects of reflection, scattering, and IT and lee-wave generation, as well as amplification of IW and IT. To properly account for the effects of depth-dependent stratification variability, further research would benefit from site specific climatology data.

Results could be further improved through increased sampling consistency between instruments (there were maintenance periods and instrument redeployments during analysis years), additional instrument sites (along the length of the canyon floor and rim), and additional overlapping comparison years between sites. Broader temporal coverage could provide insight into decadal seasonality, while additional spatial coverage would allow for observations of IW propagation. For NI wind forcing, reanalysis wind data may have provided better (fewer gaps) temporal coverage for comparison. Further research is required to: identify forcing for the periodicity of the shoaling up-canyon mean currents at Axis and the sub-diurnal range's intermittent seasonality; accurately identify sites of origin for incident baroclinic shelf-waves and IT affecting the diurnal and semidiurnal responses; better quantify the downward propagation of NI IW energy from the ML to the interior; and, improve power law fits of dissipation and near- N spectral shoulder energy to better model the cascade of energy from low- to high-frequency turbulent mixing.

Barkley Canyon is a dynamic continental slope and submarine canyon region with physical processes that are heavily influenced by topography. Slopes and canyons are known as hot-spots for IT generation and IW-driven turbulence, contributing significantly to regional transport of energy, shelf productivity, and even large-scale ocean circulation and climate effects. As regional currents, tides, and wind all contribute to an energetic local IW field, the Barkley Canyon portion of ONC's NEPTUNE cabled observatory is an important data

network for understanding the effects of topography-IW interactions on the VICS. Furthermore, results here may be valuable for characterising mixing processes at other slope and canyon sites, and for better estimating the global IW and IT energy budget. It is hoped that this study has provided valuable insight leading to further research and collaboration, and improved knowledge of the importance of shelf-incising canyon regions as fundamental to both regional and large-scale physical ocean processes.

8 Appendix A: Supplemental plots

8.1 Wind comparisons

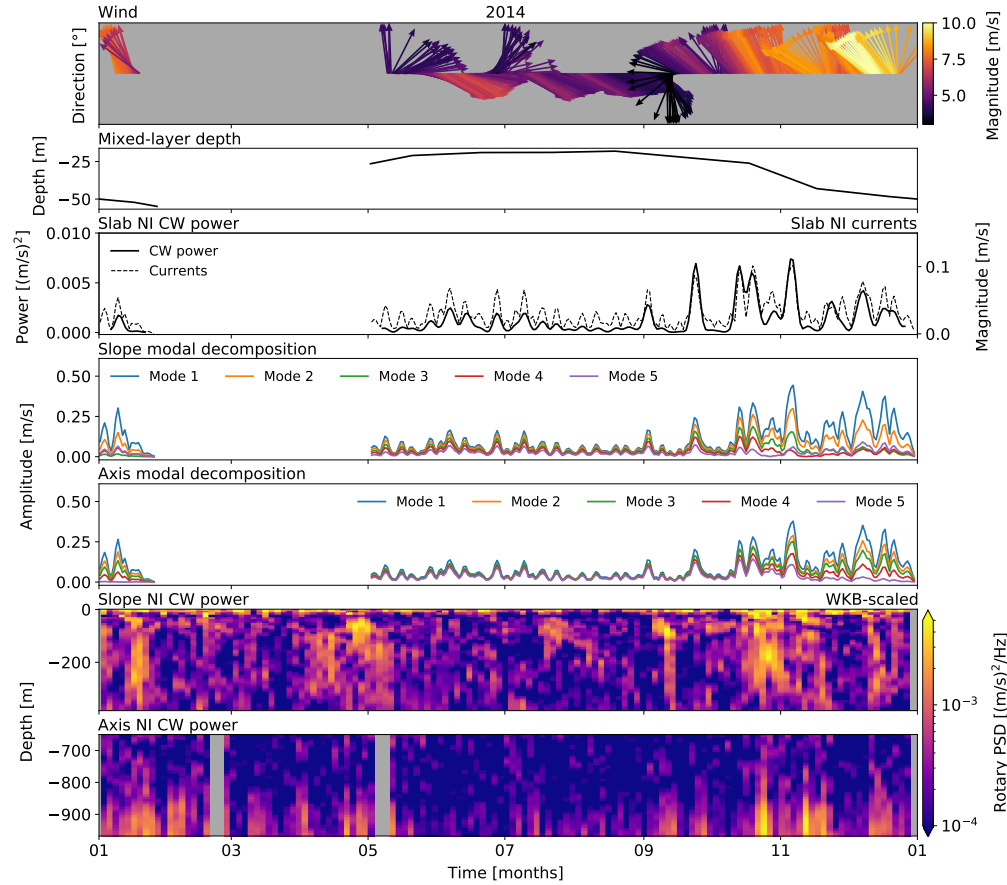


Figure 32. NI forcing analysis for 2014. Panels are (i) wind direction and amplitude, (ii) monthly-averaged ML depth for Line P station 3 as determined by Li et al. (2005), (iii) slab model NI CW power and NI currents, (iv, v) seasonal mode amplitudes for Slope and Axis, and (vi, vii) band-integrated NI CW power at Slope and Axis. There appears to be a complex relationship between the wind, ML, slab currents, and mode amplitudes in driving the NI observations, with the most obvious effects in the fall.

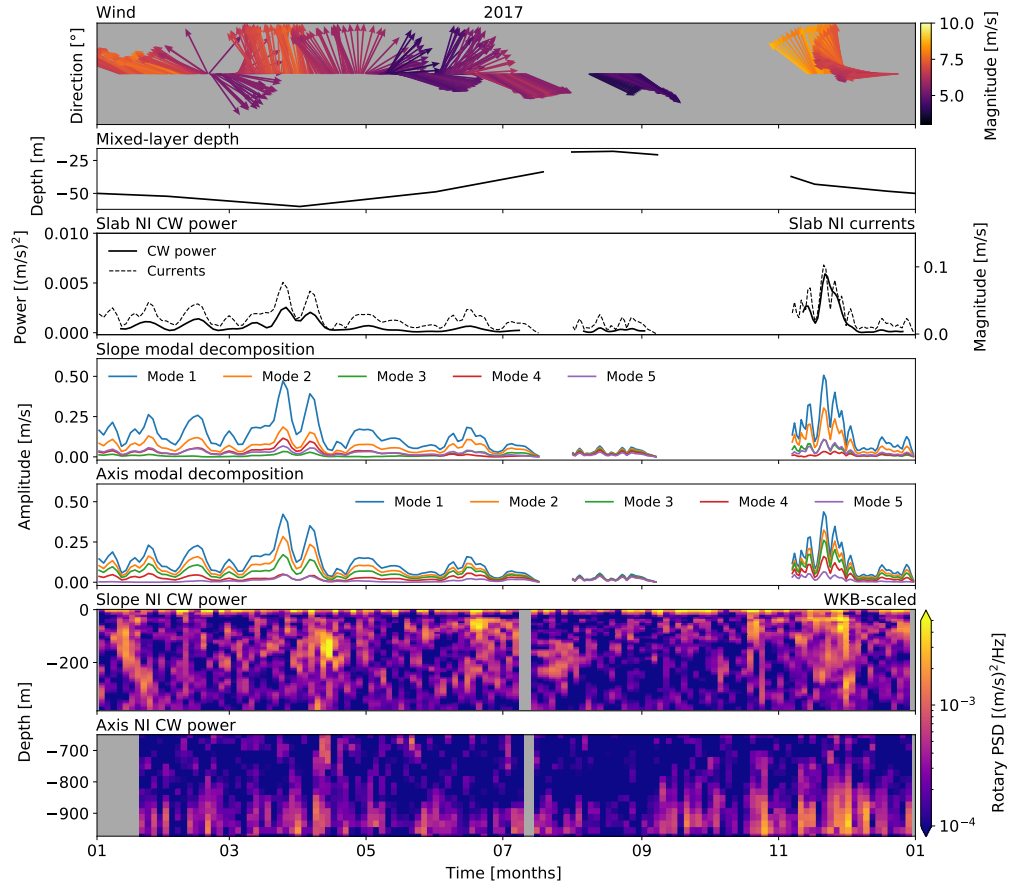


Figure 33. NI forcing analysis for 2017. Panels are (i) wind direction and amplitude, (ii) monthly-averaged ML depth for Line P station 3 as determined by Li et al. (2005), (iii) slab model NI CW power and NI currents, (iv, v) seasonal mode amplitudes for Slope and Axis, and (vi, vii) band-integrated NI CW power at Slope and Axis. There appears to be a complex relationship between the wind, ML, slab currents, and mode amplitudes in driving the NI observations, with the most obvious effects in the fall.

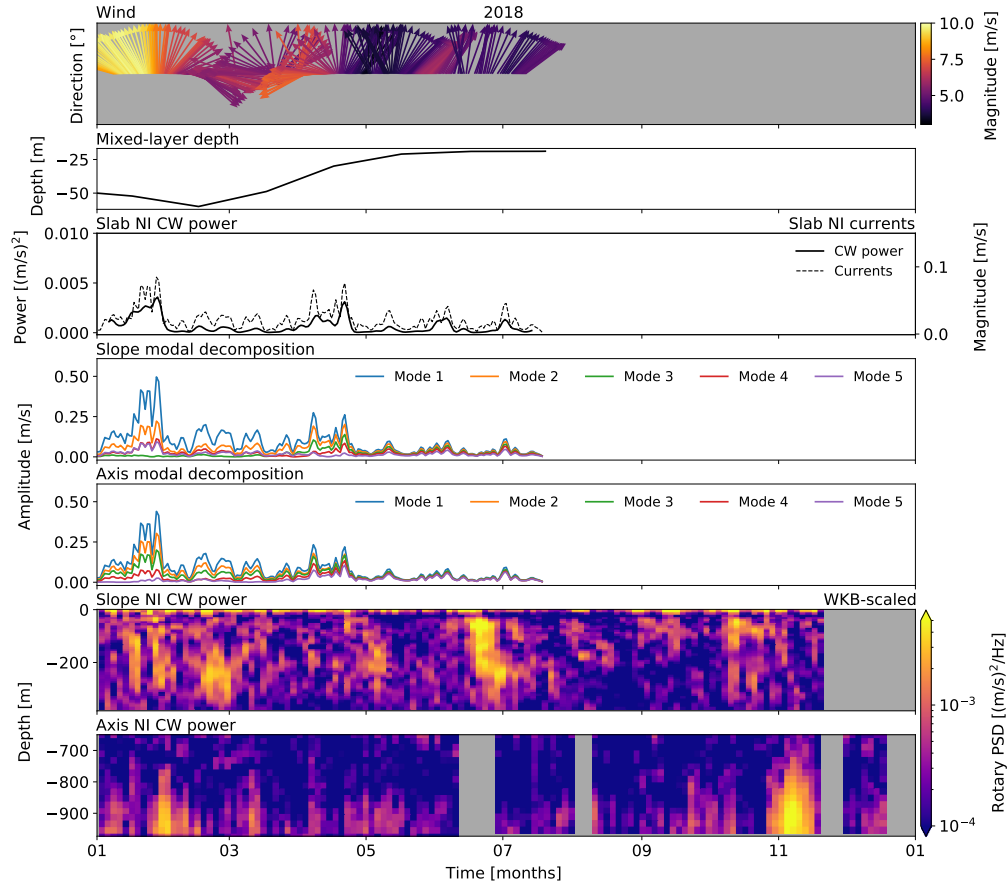


Figure 34. NI forcing analysis for 2018. Panels are (i) wind direction and amplitude, (ii) monthly-averaged ML depth for Line P station 3 as determined by Li et al. (2005), (iii) slab model NI CW power and NI currents, (iv, v) seasonal mode amplitudes for Slope and Axis, and (vi, vii) band-integrated NI CW power at Slope and Axis. There appears to be a complex relationship between the wind, ML, slab currents, and mode amplitudes in driving the NI observations, with the most obvious effects in the fall.

9 References

- Alford, M. H. (2001). Internal swell generation: The spatial distribution of energy flux from the wind to mixed layer near-inertial motions. *Journal of Physical Oceanography*, 31(8 PART 2), 2359–2368. <https://doi.org/10.1175/1520-0485>
- Alford, M. H., MacKinnon, J. A., Zhao, Z., Pinkel, R., Klymak, J., & Peacock, T. (2007). Internal waves across the Pacific. *Geophysical Research Letters*, 34(24), 24601. <https://doi.org/10.1029/2007GL031566>
- Alford, M. H. (2003). Improved global maps 54-year history of wind-work on ocean inertial motions. *Geophysical Research Letters*, 30(8), 1424. <https://doi.org/10.1029/2002GL016614>
- Alford, M. H. (2020). Revisiting near-inertial wind work: Slab models, relative stress, and mixed layer deepening. *Journal of Physical Oceanography*, 50(11), 3141–3156. <https://doi.org/10.1175/JPO-D-20-0105.1>
- Alford, M. H., Cronin, M. F., & Klymak, J. M. (2012). Annual cycle and depth penetration of wind-generated near-inertial internal waves at ocean station papa in the northeast pacific. *Journal of Physical Oceanography*, 42(6), 889–909. <https://doi.org/10.1175/JPO-D-11-092.1>
- Alford, M. H., Mackinnon, J. A., Simmons, H. L., & Nash, J. D. (2016). Near-Inertial Internal Gravity Waves in the Ocean. *Annual Review of Marine Science*, 8, 95–123. <https://doi.org/10.1146/annurev-marine-010814-015746>
- Alford, M. h., Shcherbina, A. Y., & Gregg, M. C. (2013). Observations of Near-Inertial Internal Gravity Waves Radiating from a Frontal Jet. *Journal of Physical Oceanography*, 43(6), 1209–1224. <https://doi.org/10.1175/JPO-D-12-0146.1>
- Alford, M. H., & Zhao, Z. (2007). Global patterns of low-mode internal-wave propagation. Part I: Energy and energy flux. *Journal of Physical Oceanography*, 37(7), 1829–1848. <https://doi.org/10.1175/JPO3085.1>
- Allen, S. E., Vindeirinho, C., Thomson, R. E., Foreman, M. G. G., & Mackas, D. L. (2001). Physical and biological processes over a submarine canyon during an upwelling event. *Canadian Journal of Fisheries and Aquatic Sciences*, 58(4), 671–684. <https://doi.org/10.1139/f01-008>
- Althaus, A. M., Kunze, E., & Sanford, T. B. (2003). Internal tide radiation from Mendocino escarpment. *Journal of Physical Oceanography*, 33(7),

- 1510–1527. <https://doi.org/10.1175/1520-0485>
- Anstey, K. (2022). Internal waves at Barkley Canyon. Retrieved from GitHub website: https://github.com/kurtisanstey/internal_waves_barkley_canyon
- Arbic, B. K., Richman, J. G., Shriver, J. F., Timko, P. G., Joseph Metzger, E., & Wallcraft, A. J. (2012). Global modeling of internal tides within an eddying ocean general circulation model. *Oceanography*, 25(2), 20–29. <https://doi.org/10.5670/oceanog.2012.38>
- Brink, K. H. (1991). Coastal-trapped waves and wind-driven currents over the continental shelf. *Annual Review of Fluid Mechanics*, 23(1), 389–412. <https://doi.org/10.1146/annurev.fl.23.010191.002133>
- Burrier, D. A. (2019). The Internal Wave Dynamics of Barkley Submarine Canyon. San Jose State University.
- Cabrera, F., Ogata, B., Sastri, A. R., Heesemann, M., Mihály, S., Galbraith, M., & Morley, M. G. (2018). High-frequency observations from a deep-sea cabled observatory reveal seasonal overwintering of *Neocalanus* spp. in Barkley Canyon, NE Pacific: Insights into particulate organic carbon flux. *Progress in Oceanography*, 169, 120–137. <https://doi.org/10.1016/j.pocean.2018.06.001>
- Carter, G. S., & Gregg, M. C. (2002). Intense, variable mixing near the head of Monterey Submarine Canyon. In *Journal of Physical Oceanography* (Vol. 32). <https://doi.org/10.1175/1520-0485>
- Chauvet, P., Metaxas, A., Hay, A. E., & Matabos, M. (2018). Annual and seasonal dynamics of deep-sea megafaunal epibenthic communities in Barkley Canyon (British Columbia, Canada): A response to climatology, surface productivity and benthic boundary layer variation. *Progress in Oceanography*, 169, 89–105. <https://doi.org/10.1016/j.pocean.2018.04.002>
- Crawford, W. R., & Thomson, R. E. (1984). Diurnal-Period Continental Shelf Waves along Vancouver Island: A Comparison of Observations with Theoretical Models. *Journal of Physical Oceanography*, 14(10), 1629–1646. <https://doi.org/10.1175/1520-0485>
- Cummins, P. F., Masson, D., & Foreman, M. G. G. (2000). Stratification and mean flow effects on diurnal tidal currents off Vancouver Island. *Journal of Physical Oceanography*, 30(1), 15–30. <https://doi.org/10.1175/1520-0485>
- Cummins, P. F., & Oey, L. Y. (1997). Simulation of barotropic and baroclinic

- tides off northern British Columbia. *Journal of Physical Oceanography*, 27(5), 762–781. <https://doi.org/10.1175/1520-0485>
- D'Asaro, E. A. (1985). The energy flux from the wind to near-inertial motions in the surface mixed layer. *J. Phys. Oceanogr.*, 15(8, Aug. 1985), 1043–1059. <https://doi.org/10.1175/1520-0485>
- D'Asaro, E. A. (1995). Upper-ocean inertial currents forced by a strong storm. Part III: interaction of inertial currents and mesoscale eddies. *Journal of Physical Oceanography*, 25(11 Part II), 2953–2958. <https://doi.org/10.1175/1520-0485>
- D'Asaro, E. A., Lien, R. C., & Henyey, F. (2007). High-frequency internal waves on the Oregon continental shelf. *Journal of Physical Oceanography*, 37(7), 1956–1967. <https://doi.org/10.1175/JPO3096.1>
- Doya, C., Aguzzi, J., Pardo, M., Matabos, M., Company, J. B., Costa, C., ... Canals, M. (2014). Diel behavioral rhythms in sablefish (*Anoplopoma fimbria*) and other benthic species, as recorded by the Deep-sea cabled observatories in Barkley canyon (NEPTUNE-Canada). *Journal of Marine Systems*, 130, 69–78. <https://doi.org/10.1016/j.jmarsys.2013.04.003>
- Drakopoulos, P. G., & Marsden, R. F. (1993). The internal tide off the west coast of Vancouver Island. *Journal of Physical Oceanography*, 23(4), 758–775. <https://doi.org/10.1175/1520-0485>
- Flather, R. A. (1988). A numerical model investigation of tides and diurnal-period continental shelf waves along Vancouver Island. *J. Phys. Oceanogr.*, 18(1, Jan. 1988), 115–139. <https://doi.org/10.1175/1520-0485>
- Garrett, C., & Kunze, E. (2007). Internal tide generation in the deep ocean. *Annual Review of Fluid Mechanics*, 39, 57–87. <https://doi.org/10.1146/annurev.fluid.39.050905.110227>
- Garrett, C. (2005). 2004 Program of Study: Tides Course Lectures Fellows Project Reports.
- Gemmrich, J., & Klymak, J. M. (2015). Dissipation of internal wave energy generated on a critical slope. *Journal of Physical Oceanography*, 45(9), 2221–2238. <https://doi.org/10.1175/JPO-D-14-0236.1>
- Gill, A. E. (1984). On the Behavior of Internal Waves in the Wakes of Storms. *Journal of Physical Oceanography*, 14(7), 1129–1151. <https://doi.org/10.1175/1520-0485>

- Gonella, J. (1972). A rotary-component method for analysing meteorological and oceanographic vector time series. In Deep-Sea Research and Oceanographic Abstracts (Vol. 19). <https://doi.org/10.1016/0011-7471>
- Gregg, M. C. (1989). Scaling turbulent dissipation in the thermocline. *Journal of Geophysical Research*, 94(C7), 9686. <https://doi.org/10.1029/jc094ic07p09686>
- Hotchkiss, F. S., & Wunsch, C. (1982). Internal waves in Hudson Canyon with possible geological implications. *Deep Sea Research Part A, Oceanographic Research Papers*, 29(4), 415–442. <https://doi.org/10.1016/0198-0149>
- Jarosz, E., Hallock, Z. R., & Teague, W. J. (2007). Near-inertial currents in the DeSoto Canyon region. *Continental Shelf Research*, 27(19), 2407–2426. <https://doi.org/10.1016/j.csr.2007.06.014>
- Juniper, S. K., Matabos, M., Mihály, S., Ajayamohan, R. S., Gervais, F., & Bui, A. O. V. (2013). A year in Barkley Canyon: A time-series observatory study of mid-slope benthos and habitat dynamics using the NEPTUNE Canada network. *Deep-Sea Research Part II: Topical Studies in Oceanography*, 92, 114–123. <https://doi.org/10.1016/j.dsr2.2013.03.038>
- Käse, R. H., & Allyn Clarke, R. (1978). High frequency internal waves in the upper thermocline during GATE. *Deep-Sea Research*, 25(9), 815–825. <https://doi.org/10.1016/0146-6291>
- Klymak, J. M., Alford, M. H., Pinkel, R., Lien, R. C., Yang, Y. J., & Tang, T. Y. (2011). The breaking and scattering of the internal tide on a continental slope. *Journal of Physical Oceanography*, 41(5), 926–945. <https://doi.org/10.1175/2010JPO4500.1>
- Klymak, J. M., Moum, J. N., Nash, J. D., Kunze, E., Girton, J. B., Carter, G. S., ... Gregg, M. C. (2006). An estimate of tidal energy lost to turbulence at the Hawaiian Ridge. *Journal of Physical Oceanography*, 36(6), 1148–1164. <https://doi.org/10.1175/JPO2885.1>
- Kundu, P. K., & Cohen, I. (2008). Fluid mechanics. (4th ed.). Academic Press.
- Kunze, E. (1985). Near-Inertial Wave Propagation In Geostrophic Shear. *Journal of Physical Oceanography*, 15(5), 544–565. <https://doi.org/10.1175/1520-0485>
- Kunze, E. (2017). Internal-wave-driven mixing: Global geography and bud-

- gets. *Journal of Physical Oceanography*, 47(6), 1325–1345. <https://doi.org/10.1175/JPO-D-16-0141.1>
- Kunze, E., Mackay, C., Mcphee-Shaw, E. E., Morrice, K., Girton, J. B., & Terker, S. R. (2012). Turbulent mixing and exchange with interior waters on sloping boundaries. *Journal of Physical Oceanography*, 42(6), 910–927. <https://doi.org/10.1175/JPO-D-11-075.1>
- Kunze, E., Rosenfeld, L. K., Carter, G. S., & Gregg, M. C. (2002). Internal waves in Monterey Submarine Canyon. *Journal of Physical Oceanography*, 32(6), 1890–1913. <https://doi.org/10.1175/1520-0485>
- Lamb, K. G. (2014). Internal wave breaking and dissipation mechanisms on the continental slope/shelf. *Annual Review of Fluid Mechanics*, 46, 231–254. <https://doi.org/10.1146/annurev-fluid-011212-140701>
- Lavelle, J. W., & Cannon, G. A. (2001). On subinertial oscillations trapped by the Juan de Fuca Ridge, northeast Pacific. In *Journal of Geophysical Research: Oceans* (Vol. 106). <https://doi.org/10.1029/2001jc000865>
- Leder, N. (2002). Wind-induced internal wave dynamics near the Adriatic shelf break. In *Continental Shelf Research* (Vol. 22). <https://doi.org/10.1016/S0278-4343>
- Levine, M. D. (2002). A modification of the Garrett-Munk internal wave spectrum. *Journal of Physical Oceanography*, 32(11), 3166–3181. <https://doi.org/10.1175/1520-0485>
- Li, M., Myers, P. G., & Freeland, H. (2005). An examination of historical mixed layer depths along Line P in the Gulf of Alaska. *Geophysical Research Letters*, 32(5), 1–4. <https://doi.org/10.1029/2004GL021911>
- Martini, K. I., Alford, M. H., Kunze, E., Kelly, S. M., & Nash, J. D. (2011). Observations of internal tides on the oregon continental slope. *Journal of Physical Oceanography*, 41(9), 1772–1794. <https://doi.org/10.1175/2011JPO4581.1>
- Martini, K. I., Alford, M. H., Kunze, E., Kelly, S. M., & Nash, J. D. (2013). Internal bores and breaking internal tides on the Oregon continental slope. *Journal of Physical Oceanography*, 43(1), 120–139. <https://doi.org/10.1175/JPO-D-12-030.1>
- Mihaly, S. F., Thomson, R. E., & Rabinovich, A. B. (1998). Evidence for non-linear interaction between internal waves of inertial and semidiurnal frequency. *Geophysical Research Letters*, 25(8), 1205–1208. <https://doi.org/>

/10.1029/98GL00722

- Morozov, E. G. (2018). Semidiurnal Internal Wave Global Field; Global Estimates of Internal Tide Energy. In *Oceanic Internal Tides: Observations, Analysis and Modeling* (pp. 263-291). https://doi.org/10.1007/978-3-319-73159-9_8
- Munk, W., & Garrett, C. (1979). Internal Waves and Small-Scale Processes. In C. Wunsch (Ed.), *Evolution of Physical Oceanography*.
- Munk, W., & Wunsch, C. (1998). Abyssal recipes II: Energetics of tidal and wind mixing. *Deep-Sea Research Part I: Oceanographic Research Papers*, 45(12), 1977–2010. <https://doi.org/10.1016/S0967-0637>
- Nash, J. D., Kunze, E., Toole, J. M., & Schmitt, R. W. (2004). Internal tide reflection and turbulent mixing on the continental slope. In *Journal of Physical Oceanography* (Vol. 34). <https://doi.org/10.1175/1520-0485>
- Petruncio, E. T., Rosenfeld, L. K., & Paduan, J. D. (1998). Observations of the internal tide in Monterey Canyon. *Journal of Physical Oceanography*, 28(10), 1873–1903. <https://doi.org/10.1175/1520-0485>
- Pinkel, R. (1975). Upper ocean internal wave observations from Flip. *Journal of Geophysical Research*, 80(27), 3892–3910. <https://doi.org/10.1029/jc080i027p03892>
- Pinkel, R. (2014). Vortical and internal wave shear and strain. *Journal of Physical Oceanography*, 44(8), 2070–2092. <https://doi.org/10.1175/JPO-D-13-090.1>
- Polzin, K. L., & Lvov, Y. V. (2011). Toward regional characterizations of the oceanic internal wavefield. *Reviews of Geophysics*, 49(4), 4003. <https://doi.org/10.1029/2010RG000329>
- Polzin, K. L., Toole, J. M., Ledwell, J. R., & Schmitt, R. W. (1997). Spatial variability of turbulent mixing in the abyssal ocean. *Science*, 276(5309), 93–96. <https://doi.org/10.1126/science.276.5309.93>
- Polzin, K. (2004). A heuristic description of internal wave dynamics. *Journal of Physical Oceanography*, 34(1), 214–230. <https://doi.org/10.1175/1520-0485>
- Robertson, R., Dong, J., & Hartlipp, P. (2017). Diurnal Critical Latitude and the Latitude Dependence of Internal Tides, Internal Waves, and Mixing Based on Barcoo Seamount. *Journal of Geophysical Research: Oceans*, 122(10), 7838–7866. <https://doi.org/10.1002/2016JC012591>

- Rudnick, D. L., Gopalakrishnan, G., & Cornuelle, B. D. (2015). Cyclonic eddies in the Gulf of Mexico: Observations by underwater gliders and simulations by numerical model. *Journal of Physical Oceanography*, 45(1), 313–326. <https://doi.org/10.1175/JPO-D-14-0138.1>
- Sun, H., & Kunze, E. (1999). Internal wave-wave interactions. Part I: The role of internal wave vertical divergence. *Journal of Physical Oceanography*, 29(11), 2886–2904. <https://doi.org/10.1175/1520-0485>
- Terker, S. R., Girton, J. B., Kunze, E., Klymak, J. M., & Pinkel, R. (2014). Observations of the internal tide on the California continental margin near Monterey Bay. *Continental Shelf Research*, 82, 60–71. <https://doi.org/10.1016/j.csr.2014.01.017>
- Thomson, R. E., & Crawford, W. R. (1982). The Generation of Diurnal Period Shelf Waves by Tidal Currents in: *Journal of Physical Oceanography* Volume 12 Issue 7 (1982). *Journal of Physical Oceanography*, 12(7). Retrieved from https://journals-ametsoc-org.ezproxy.library.uvic.ca/view/journals/phoc/12/7/1520-0485_1982_012_0635_tgodps_2_0_co_2.xml?tab_body=pdf
- Thomson, R. E., & Emery, W. J. (2014). Data Analysis Methods in Physical Oceanography: Third Edition. In *Data Analysis Methods in Physical Oceanography: Third Edition (Third)*. <https://doi.org/10.1016/C2010-0-66362-0>
- Thomson, R. E., & Fine, I. V. (2003). Estimating mixed layer depth from oceanic profile data. *Journal of Atmospheric and Oceanic Technology*, 20(2), 319–329. <https://doi.org/10.1175/1520-0426>
- Thomson, R. E., & Krassovski, M. V. (2015). Remote alongshore winds drive variability of the California Undercurrent off the British Columbia-Washington coast. *Journal of Geophysical Research: Oceans*, 120(12), 8151–8176. <https://doi.org/10.1002/2015JC011306>
- Thomson, R. E., Roth, S. E., & Dymond, J. (1990). Near-inertial motions over a mid-ocean ridge: Effects of topography and hydrothermal plumes. *Journal of Geophysical Research*, 95(C5), 7261. <https://doi.org/10.1029/jc095ic05p07261>
- Voelker, G. S., Olbers, D., Walter, M., Mertens, C., & Myers, P. G. (2020). Estimates of wind power and radiative near-inertial internal wave flux: The hybrid slab model and its application to the North Atlantic. *Ocean Dynamics*, 70(11), 1357–1376. <https://doi.org/10.1007/s10236-020-01388-y>

- Waterhouse, A. F., Mackinnon, J. A., Musgravea, R. C., Kelly, S. M., Pickering, A., & Nash, J. (2017). Internal tide convergence and mixing in a submarine canyon. *Journal of Physical Oceanography*, 47(2), 303–322. <https://doi.org/10.1175/JPO-D-16-0073.1>
- Xie, X., & Chen, D. (2021). Near-surface reflection and nonlinear effects of low-mode internal tides on a continental slope. *Journal of Physical Oceanography*, 51(4), 1037–1051. <https://doi.org/10.1175/JPO-D-20-0197.1>
- Xu, J. P., & Noble, M. A. (2009). Currents in monterey submarine canyon. *Journal of Geophysical Research: Oceans*, 114(3), 3004. <https://doi.org/10.1029/2008JC004992>
- Zervakis, V., & Levine, M. D. (1995). Near-inertial energy propagation from the mixed layer: theoretical considerations. *Journal of Physical Oceanography*, 25(11 Part II), 2872–2889. <https://doi.org/10.1175/1520-0485>
- Zhai, X., Greatbatch, R. J., & Zhao, J. (2005). Enhanced vertical propagation of storm-induced near-inertial energy in an eddying ocean channel model. *Geophysical Research Letters*, 32(18), 1–4. <https://doi.org/10.1029/2005GL023643>
- Zhao, Z., Alford, M. H., Girton, J. B., Rainville, L., & Simmons, H. L. (2016). Global observations of open-ocean mode-1 M2 internal tides. *Journal of Physical Oceanography*, 46(6), 1657–1684. <https://doi.org/10.1175/JPO-D-15-0105.1>
- Zheng, J., Tian, J., & Liang, H. (2017). Observation of near-inertial internal waves on the continental slope in the northwestern South China Sea. *Journal of Ocean University of China*, 16(2), 184–190. <https://doi.org/10.1007/s11802-017-3153-7>